



Lawrence Berkeley Laboratory

UNIVERSITY OF CALIFORNIA

ENERGY & ENVIRONMENT DIVISION

Submitted to Solar Energy

AN EMPIRICAL METHOD FOR ESTIMATING THE THERMAL
RADIANCE OF CLEAR SKIES

Paul Berdahl and Richard Fromberg

May 1981

TWO-WEEK LOAN COPY

*This is a Library Circulating Copy
which may be borrowed for two weeks.
For a personal retention copy, call
Tech. Info. Division, Ext. 6782*



DISCLAIMER

This document was prepared as an account of work sponsored by the United States Government. While this document is believed to contain correct information, neither the United States Government nor any agency thereof, nor the Regents of the University of California, nor any of their employees, makes any warranty, express or implied, or assumes any legal responsibility for the accuracy, completeness, or usefulness of any information, apparatus, product, or process disclosed, or represents that its use would not infringe privately owned rights. Reference herein to any specific commercial product, process, or service by its trade name, trademark, manufacturer, or otherwise, does not necessarily constitute or imply its endorsement, recommendation, or favoring by the United States Government or any agency thereof, or the Regents of the University of California. The views and opinions of authors expressed herein do not necessarily state or reflect those of the United States Government or any agency thereof or the Regents of the University of California.

AN EMPIRICAL METHOD FOR ESTIMATING
THE THERMAL RADIANCE OF CLEAR SKIES†

Paul Berdahl and Richard Fromberg‡

Lawrence Berkeley Laboratory

University of California

Berkeley CA 94720

ABSTRACT

Measurements of the longwave radiance of the sky were made during the summer of 1979 at Tucson, Arizona; Gaithersburg, Maryland; and St. Louis, Missouri. The global longwave radiation (wavelengths greater than 3 microns) was monitored with a pyrgeometer and the distribution of this radiation in several spectral bands at five different zenith angles was monitored with a spectral radiometer. This paper presents results for the global sky radiation during clear sky conditions. The spectral radiometer was used to calibrate the pyrgeometer and to detect the presence of clouds. The results can most appropriately be summarized in terms of the correlation between the global sky emissivity ϵ_{sky} and surface dewpoint temperature T_{dp} ($^{\circ}\text{C}$). The global sky emissivity is defined as the ratio of sky radiance to σT_a^4 , where T_a is the absolute air temperature near the ground, and σ is the Stefan-Boltzmann constant. Based

† This work was supported by the Assistant Secretary for Conservation and Renewable Energy, Office of Solar Applications for Buildings, Passive and Hybrid Division of the U.S. Department of Energy, under Contract No. W-7405-ENG-48.

‡ Present address: Pacific Gas and Electric Company, San Francisco, CA 94106, U.S.A.

on 2945 nighttime measurements in all three cities we find

$$\epsilon_{\text{sky}} = 0.741 + 0.0062 T_{\text{dp}}$$

with a standard error of estimate of 0.031. A similar relationship with almost identical coefficients holds during daylight hours. Although the primary emphasis of this paper is the thermal radiance of clear skies, methods are recommended for correcting for cloud cover and performing a simple estimate of the spectral distribution of the radiation.

1. INTRODUCTION

As emphasized by Trombe[1], Head[2], Catalanotti et al. [3], and Addeo et al. [4], the use of the cold sky as a heat sink for radiating bodies on the earth's surface may provide a promising alternative to conventional cooling techniques. If the emitted radiation of a surface exceeds the absorbed radiation, the surface will cool. The effective "sky temperature" is almost invariably lower than the ambient temperature because the atmospheric temperature decreases with elevation and the atmosphere is partly transparent to radiation of certain wavebands within the infrared region of the spectrum. On a planetary scale, the infrared exchanges between the earth and sky and between the atmosphere and space allow the earth to maintain an equilibrium temperature by emitting the great quantities of heat gained each day from the sun.

A quantitative understanding of sky radiation is necessary for the design of radiant cooling systems. For example, the ability to predict sky radiation accurately, along with a knowledge of the radiative and other heat transfer characteristics of surfaces, can be used to help design buildings which remain cool without mechanical conditioners. In addition to radiative cooling applications, an accurate model of sky radiation is desirable for predicting radiative losses from the covers of solar collectors and the exposed surfaces of buildings.

The sky's thermal radiation during the summer at midlatitudes is typically 400Wm^{-2} . A 5% error in measurement or estimation of this radiation (difficult to achieve) represents 20Wm^{-2} . Yet the net radiation loss of a surface at ambient temperature under clear skies is about 70Wm^{-2} . Thus a 5% error in determining the atmospheric radiation

represents nearly a 30% error in the net cooling power, which emphasizes the need for accurate measurements and models.

Measurements of the sky's angular and spectral radiation, as well as global radiation, have been made at six cities in the southern United States. The goal has been to obtain data for the majority of one summer at each site. We report results here for Tucson, Arizona; Gaithersburg, Maryland; and St. Louis, Missouri based on measurements during the summer of 1979 and the following winter. Additional results may be available in the future based on measurements at San Antonio, Texas; West Palm Beach, Florida; and Boulder City, Nevada.

The radiometer instrumentation systems were designed particularly to obtain extensive measurements of the angular and spectral distribution of sky radiation. However, in view of the importance and difficulty in obtaining accurate estimates of even the total (global) values of this radiation we will focus on global sky radiation for cloudless skies.

The general characteristics of sky radiation are discussed in the next section, followed by a summary of currently available techniques for estimating the thermal radiance of clear skies. After a brief description of the experimental equipment, the procedures employed in the analysis of the data are presented. These procedures consist of (i) a method for detecting the presence of clouds utilizing the sky radiance in the 8.8 micron channel, (ii) an analysis of the small day/night differences of sky emissivity, and (iii) a method for calibrating the pyrgeometer with the spectral radiometer. The experimental results are presented as correlations of sky emissivity versus surface dewpoint

temperature. The correlations can be represented by simple algebraic expressions and be used for predictions of cooling rates. Comparisons with results by earlier researchers are made. Some suggestions are presented as to how the radiance of cloudy skies should be estimated, based on our relationship for clear skies. Finally, it is shown how the global radiance within the 8 to 13 micron window can be estimated when the total sky emissivity is known.

2. CHARACTERISTICS OF THERMAL SKY RADIATION

The 5-50 micron portion of the infrared spectrum, contains most of the radiation emitted by bodies at ambient temperatures. Figure 1 shows the fraction of the energy emitted by a black body below various wavelengths for two temperatures within the ambient range. The region above 25 microns can be ignored for many purposes because the atmosphere is virtually opaque due to water vapor absorption.

Water vapor and carbon dioxide account for most of the absorption in the cloudless atmosphere. Ozone and other constituents are of secondary importance. Since Kirchhoff's law states that the absorptivity of a material must equal its emissivity at the same wavelength, the absorption due to water and carbon dioxide in the atmosphere leads to corresponding emission. The absorption spectra of H_2O , CO_2 , O_3 , and air are given in Figure 2 based on data from Ref. 5. Strong water vapor absorption bands fall below 8 microns where vibrational transitions occur. Above 13 microns lie the rotational transitions which become stronger above 20 microns. Carbon dioxide is highly absorptive from 14 to 16 microns due to vibrational transitions. Thus it is the second most important absorber even though it constitutes only 0.03% of the

atmosphere by volume. Ozone absorbs in the region from 9.4 to 9.8 microns, but plays a major role in radiative exchange only at high altitudes. A superposition of the above spectra (Fig.2d) reveals several gaps, where the atmosphere is rather transmissive. Figure 3 shows the spectral emission of several portions of the cloudless sky[6]. The zenith (0°) emission spectrum is very similar to that of a black body with the temperature of the air near the earth's surface, except for the large "hole" extending from 8 to 13 microns. This weak emission from 8 to 13 microns is caused by the "atmospheric window" apparent in the absorption spectrum in Fig.2d.

Figure 4 shows the radiance from the clear sky in the winter. Due to the smaller amounts of water vapor present the principle atmospheric window produces a deeper minimum, and a secondary window appears in the 16 to 22 micron region. For most cooling applications (warm summertime atmospheric conditions) the secondary window is unimportant; however, for very dry conditions which primarily occur in the winter, it must be included in any spectral analysis. Outside the atmospheric windows, the sky radiation is, to a good approximation, equal to that of a black body with the temperature of the air near the ground. For precise analysis, small corrections to this blackbody radiance can be introduced by considering the variation of temperature with height (lapse rate) near the ground.

The effect of clouds upon the spectrum of atmospheric radiation may be seen in Fig. 5 [6]. Clouds have been simulated as blackbody emitters, a good approximation provided the clouds are optically thick in the visible spectrum. Cloud cover has a strong effect on the atmos-

pheric radiation that decreases in importance with cloud elevation because higher clouds are usually colder than low clouds. In the portion of the analysis to follow which pertains to clear skies only, the strong infrared emission by clouds has been used to detect clouds, to enable the deletion of data obtained during cloudy periods.

The cooling rate of surfaces exposed to the sky depends upon the difference between energy emitted and that absorbed from the sky. Figure 6 shows blackbody emission spectra of surfaces at temperatures other than ambient. The radiative loss to the sky corresponds to the area under the blackbody curves minus the area under the sky spectrum, see Figure 7. Surfaces above ambient temperatures radiate most if they are black bodies. Surfaces below ambient radiate the most energy if they are emissive only between 8 and 13 microns, Figure 8. At operating radiator temperatures as low as 20°C below air temperature a selective radiator should emit only in the narrower region 8 to 12.5 microns, Figure 9. Cooling can be achieved during daylight hours if the radiator surface or its glazing can reflect solar radiation. Shading of the radiator surface can also lead to cooling during daylight hours. The maximum rate of cooling of a surface at air temperature by radiation within the 8 to 13 micron region can be found by assuming that the atmosphere produces no radiation within this band. From Fig. 1 one finds that this band contains about 30% of black body radiance. At an air temperature of 300 K (27°C) the black body radiance σT^4 is 460 Wm⁻². Thus the maximum cooling rate at 27°C is approximately 138 Wm⁻².

The primary phenomenon causing atmospheric emission in the 8 to 13 micron range is the continuum absorption. This absorption does not have

the underlying line structure of the rotational and vibrational bands of water vapor, but it is still dependent on the amount of water vapor in the atmosphere. This continuous absorption may be due to the presence of dimers[7] (bound states of two water molecules) in the atmosphere. The continuous absorption could thus be a result of the weak hydrogen bonding of the molecules, making available many different transitions when the water molecules break apart. Given so many different bound-free transitions, a continuous absorption spectrum would result. Another hypothesis is that the continuum absorption is due to the distant wings of strong water vapor absorption lines located in nearby bands[8]. Still a third hypothesis is that the continuum absorption spectrum is caused by clusters of water molecules, perhaps nucleated by atmospheric ions[9]. It is remarkable that there is no real consensus on the basic physics of the continuum absorption.

3. METHODS FOR ESTIMATING THE THERMAL RADIANCE OF CLEAR SKIES

The methods for estimating the thermal radiance of the sky fall naturally into two classes. The first class consists of empirical methods based on direct measurements of sky radiance. For example, one can use surface temperature and humidity to predict sky radiance if a suitable correlation is available. The second class utilizes the detailed profiles of atmospheric constituents, together with a knowledge of their radiative properties, to derive the atmospheric radiance. These more detailed methods are preferred in principle, although in practice they suffer from the necessity for detailed input information on the state of the atmosphere and from the absence of some of the fundamental information concerning the radiative properties of atmospheric constituents, especially the properties of water vapor in the 8 to 13 micron range.

Empirical Relations

A number of equations have been proposed in an attempt to best fit experimental measurements of clear sky radiation. The basic parameters are the partial water vapor pressure e (mb) or dewpoint T_{dp} and the surface temperature T_a . Some investigators have included temperature jumps at the surface, relative humidity, or atmospheric pressure. Detailed discussions may be found in the monographs by Geiger[10], Kondratyev[11,12], and Sellers[13]. We review several of the principal relationships below.

Angstrom's equation was introduced [15] in 1916. In our notation it reads

$$\epsilon_{\text{sky}} = A - B \exp(-C\epsilon), \quad (1)$$

where A, B, and C are empirical constants which have been assigned values in the ranges (0.75,0.82), (0.15,0.33), and (0.09,0.22), respectively. The most frequently used values, according to Kondratyev[11], are $A=0.806$, $B=0.236$, and $C=0.092$. This equation is similar to Beer's law, with $C\epsilon$ playing the role of the average optical thickness in the thermal infrared spectrum.

Another relationship often employed to characterize experimental data is that given by Brunt [15,16]:

$$\epsilon_{\text{sky}} = a + b\epsilon^{1/2}, \quad (2)$$

which is similar to Angstrom's equation (1) and preferable on the grounds that it has only two adjustable constants rather than three. The values for a fall in the range (0.34 to 0.71) and the values for b lie in the range (0.023 to 0.110). Sellers suggests the use of the median of 22 evaluations and obtains $a = 0.605$ and $b = 0.048$. Brunt obtained $a = 0.55$, $b = 0.056$, based on data collected by Dines[17]. Three studies performed after 1955[18,19,20] give values of a and b close to those found by Brunt. Brunt's argument for using the square root of the water vapor pressure is based on an analogy between heat transfer by conduction and heat transfer by radiation. (For transient conduction the average heat flux can be proportional to the square root of the heat conductivity.) In light of the modern theory of the transport of atmospheric radiation, there is no reason to expect a dependence on the square root of the water vapor pressure. In fact, the continuum water vapor absorption is primarily responsible for the variation in atmospheric emissivity with water vapor content, and this absorption

is believed to be approximately proportional to the square of the water vapor content[21]. Nevertheless, the Brunt relationship has proved quite useful for summarization of experimental data, since it can be made to fit the data reasonably well.

In section 6 we will express our experimental results in terms of the surface dewpoint temperature T_{dp} rather than the water vapor pressure. Our choice is based merely on the ease of use of the dewpoint.

Clark and Allen[22] have employed the dewpoint temperature T_{dp} ($^{\circ}\text{C}$) to summarize the results of 800 clear sky nighttime measurements at San Antonio, Texas:

$$\epsilon_{sky} = 0.787 + 0.764 \ln [(T_{dp} + 273)/273]. \quad (3)$$

This relationship is virtually linear over the range of dewpoints (-20°C to $+25^{\circ}\text{C}$) of their observations. These measurements were made recently, with modern equipment, in contrast with much of the currently available information. The standard error of estimate is about 0.025 for their observations.

Another approach to the estimation of the emissivities of cloudless skies has been advocated by Swinbank[23] and by Idso and Jackson[24]. The sky emissivity is to be estimated by means of the air temperature alone, without reference to any measure of atmospheric humidity. The general usefulness of these relations lies in the fact that the dewpoint temperature is correlated with air temperature. However, for the present work, relations based on air temperature alone are not suffi-

ciently accurate to apply in both dry and humid climates.

Detailed Methods For Estimating Sky Radiance

(a) The Use of Transmittances to Estimate Radiances.

It is desirable to estimate the sky radiance based on measured properties of the atmospheric constituents. A first principles calculation is generally impractical (partly because there are at least several thousand important spectral lines which would have to be considered). A practical strategy is to measure and compile the spectral transmittances of the atmosphere as a function of its temperature and constituents and to use Kirchhoff's law to produce corresponding radiances. Suppose one has obtained, by whatever means, the infrared transmittance $\tau(z)$ as a function of elevation z above the site for which sky radiance is to be calculated. The transmittance will generally be averaged over some spectral interval $\Delta\lambda$ about the wavelength λ for a path which need not be vertical. Atmospheric scattering can usually be neglected for thermal radiation. Under these conditions it is possible to compute the sky radiance averaged over the spectral interval $\Delta\lambda$ using the following procedure.

Let the atmosphere be divided into a number of horizontal layers by means of levels labeled 1, 2, Let $\tau_{i,j}$ be the (high resolution) transmittance between the levels i and j . By Kirchhoff's law the emission from the layer between levels n and $n+1$ is $B(\lambda, T_n)(1 - \tau_{n,n+1})$, where $B(\lambda, T_n)$ is the Planck function representing the radiance (per unit solid angle) of a black body with temperature T_n . The explicit dependence of τ upon λ has not been shown to simplify the notation. The

spectral radiance as seen at ground level is obtained by accounting for the transmittance between level n and the ground and summing over n :

$$R = \sum_{n=1}^{\infty} B(\lambda, T_n)(1 - \tau_{n,n+1}) \tau_{1,n}. \quad (4)$$

Averaging this equation over some small range of λ is now indicated but the average of the term containing two factors of τ would be very difficult to obtain. Therefore this quadratic term is eliminated by the use of the identity $\tau_{1,n} \tau_{n,n+1} = \tau_{1,n+1}$. The radiance R can consequently be written in the form

$$R = \sum_{n=1}^{\infty} B(\lambda, T_n)(\tau_{1,n} - \tau_{1,n+1}).$$

This equation can now be averaged over a small range of wavelengths about λ , with these averages denoted by bars:

$$\bar{R} = \sum_{n=1}^{\infty} B(\lambda, T_n)(\bar{\tau}_{1,n} - \bar{\tau}_{1,n+1}).$$

The Planck function was taken outside the average by using the assumption that the average will be performed over sufficiently small wavelength ranges such that the Planck function is essentially constant. To summarize the derivation of sky radiance from values of transmittance, the above equation will be restated. Let $\bar{\tau}(\lambda, z, \theta)$ be the known spectral transmittance of the atmosphere averaged about some small spectral interval about λ from ground level to elevation z in the direction given by zenith angle θ . Then the spectral radiance of the atmosphere (per unit solid angle) is given by

$$\bar{R}(\lambda, \theta) = - \int_0^{\infty} dz B(\lambda, T(z)) \frac{d\bar{\tau}(\lambda, z, \theta)}{dz}, \quad (5)$$

where B is the Planck function and $T(z)$ is the absolute temperature at

height z in the atmosphere.

(b) The Lowtran Computer Models

The LOWTRAN 3B computer code is designed to calculate the spectral transmittance of the atmosphere for a wide variety of atmospheric paths under various atmospheric conditions [25]. It can therefore be used in connection with (5) to calculate values of the spectral radiance of the sky. When these radiances are integrated over the spectrum, summed appropriately over the dome of the sky, and divided by σT_a^4 , values of the emissivity of clear skies can be obtained. These values will be compared with the results of our measurements in Section 7.

Two newer versions of LOWTRAN, LOWTRAN 4 and LOWTRAN 5, are currently available[26,27]. The new versions can compute radiances directly for the user. We believe the new programs are essentially equivalent to our procedure, since they are based on the same phenomenological description of the atmospheric transmittances.†

The LOWTRAN model calculates transmittances for a given atmospheric path by computing an "effective absorber amount" for each of the radiatively important gases. This concept is used to account for the variations in temperature and pressure along the given atmospheric path. Subsequently, empirical functions are used to obtain the reduction in transmittance due to each constituent. Gases treated in this fashion

†The LOWTRAN programs are thoroughly documented [25,26,27], and are publically available. They do have some minor shortcomings for the calculation of radiances. Ben-Shalom et al. [28] have pointed out that the program does not always properly treat (i.e., it should ignore) scattering. Also, the level spacing near the ground should be decreased from 1 km to approximately 0.1 km.

are water vapor, carbon dioxide, ozone, and a number of minor constituents important if the observer is at high altitude. Absorption due to the water vapor continuum and aerosols is included separately. The aerosol absorption usually has only a minor effect upon the computation of sky radiance[6]. One convenient aspect of the LOWTRAN models is that they contain "typical" model atmospheres, which can be used in lieu of upper-air data in suitable applications. Further description of the LOWTRAN models and comparisons with experimental data may be found in the documentation [25,26,27] and elsewhere[29,30].

(c) Flux Emissivity Models

The expression for the total, hemispherical sky radiance S is the integrated form of (5):

$$S = \int_0^{\infty} d\lambda \int d\Omega \cos\theta \bar{R}(\lambda, \theta), \quad (6)$$

where Ω represents solid angle. Bliss[31], Atwater and Ball[32], and Exell[33] employ a flux emissivity form for S written in the form

$$S = \int_0^{\infty} dz \sigma T^4(z) \frac{d \epsilon_F(z)}{dz}, \quad (7)$$

where $\epsilon_F(z)$ is the flux emissivity defined by

$$\epsilon_F(z) = \frac{-1}{\sigma T^4(z)} \int_0^{\infty} d\lambda B(\lambda, T(z)) \int d\Omega \cos\theta [1 - \bar{\tau}(\theta, z, \lambda)]. \quad (8)$$

For an isothermal layer lying between height zero and height z , the flux emissivity represents the ratio of emitted flux to that produced by a black body at the same temperature. It is assumed that $\epsilon_F(z)$ is independent of temperature, except through implicit dependence in $\bar{\tau}$, and consequently the derivative of the flux emissivity with height can

be written

$$\frac{d\epsilon_F(z)}{dz} = \frac{1}{\sigma T^4(z)} \int_0^{\infty} d\lambda B(\lambda, T(z)) \int d\Omega \cos\theta \frac{d\tau(\theta, z, \lambda)}{dz}. \quad (9)$$

That is, terms arising from the differentiation of $1/T^4(z)$ are assumed to approximately cancel terms arising from the differentiation of $B(\lambda, T(z))$. Equations (7) and (9) can be easily seen as equivalent to eqns (5) and (6) for calculations of the sky radiance. One does not, however, use (9) to compute the flux emissivity, but uses the definition (8) instead. Therefore the flux emissivity methods introduce an approximation of weak temperature dependence not required if spectral transmittance values are available for direct use in eqn (5). Each of the flux emissivity methods for computing sky radiance includes a simplified prescription for computing the flux emissivities as functions of the amounts of water vapor, carbon dioxide, and ozone. The results of Atwater and Ball[32], and those of Exell[33] are presented for average sky conditions which include clouds. The results of Bliss[31] and those of Staley and Jurica[34] include explicit results for clear skies and their results will be used for comparison with our own in Section 7.

4. INSTRUMENTATION

Each test site was equipped with a spectral radiometer for angular and spectral measurements of sky radiation, a pyrgeometer for global measurements of atmospheric thermal flux, ambient and dewpoint temperature sensors, and a rain detector. The instrumentation is controlled by a microcomputer data acquisition system. Accumulated data was transferred to our laboratory at intervals of one to three days by means of a MODEM and standard telephone lines.

The spectral radiometer is based on the 12-880 model instrument manufactured by Barnes Engineering Corporation fitted with six bandpass filters. The halfpower cuton and cutoff points of the filters are given in microns by (8.1,13.7), (8.3,9.1), (9.4,9.9), (10.0,11.4), (14.0,15.8), and (16.6,21.6). These filters are referred to as the 8 to 14, 8.8, 9.6, 11, 15, and 17 to 22 micron filters. There are also open and closed positions of the filter wheel; the closed position is used to monitor the instrument's offset.

The spectral radiometer has a field of view 2 degrees wide (full width at half maximum). The measurement direction is controlled by a rotating mirror assembly which permits the instrument to view an arc between the zenith and the north horizon. Every half hour, measurements are made with each filter for zenith angles of 0, 20, 40, 60, and 80 degrees. A blackbody reference is viewed after each set of measurements. Calibration of the spectral radiometer is accomplished by varying the blackbody temperature between ambient and 70°C during the course of a day's measurements. The blackbody measurements are then subjected to a least squares fitting procedure to determine calibration constants

and mirror corrections for each filter channel. The temperatures of the blackbody and of the mirror are measured for use during the calibration procedure. The accuracy of the radiometer, referred to a blackbody with a temperature of about 25°C is better than $\pm 2^\circ\text{C}$. The corresponding random error of measurement is less than 0.7°C in all channels. Measurements made with the spectral radiometer were compared with calculated values obtained from eqn (5) and LOWTRAN 3B atmospheric transmittances. Good agreement was found in all spectral bands[29]. The agreement of the LOWTRAN model with spectral radiometer measurements thus provides independent evidence that the spectral radiometer has been accurately calibrated.

The Eppley model PIR pyrgeometer is employed to obtain the global measurements of thermal sky radiance. It is a thermopile instrument, similar to a solar pyranometer, but with a silicon dome in place of the usual glass pyranometer dome. The silicon dome is coated with a multilayer interference filter to make the silicon opaque at wavelengths less than 3 microns. An approximate transmission spectrum of the dome is given in Fig. 10. Most of the spectral features in this plot can be identified with the intrinsic lattice absorption of the silicon. The radiative cooling rate of the sensitive surface of the pyrgeometer causes the thermopile to produce an output voltage. In order that the instrument may produce an output voltage proportional to the downcoming thermal sky radiance, an internal analog circuit produces a voltage proportional to σT^4 , where T is the absolute temperature of the instrument. This voltage is added in series with the thermopile output (with

appropriate sign) to produce the instrument's output signal.

5. ANALYSIS OF THE SKY RADIATION DATA

Three aspects of the data analysis merit an explicit discussion. A test was developed, using the 8.8 micron spectral radiance data, to detect clouds. It was used to limit the sky emissivity versus dewpoint analysis to clear skies only. Because the spectral radiometer was well calibrated, it was used to calibrate the pyrgeometer, using measured radiances from the open hole channel. Finally, an error analysis of the pyrgeometer was performed to delineate the limitations of the calibration procedure.

Detection of Clouds

To a good approximation, clouds may be considered grey-body sources of radiation. Thick clouds radiate as black bodies. Most low level (1 km) and middle level (4 km) clouds are thick enough to radiate as black bodies. High clouds (10 km) are typically thin and cold and are thus difficult to detect by infrared methods. They contribute little to the sky radiance at ground level, however, and their detection is thus not essential. According to Sellers [13], the ratio of cloudy to clear sky total radiation varies roughly from 1.04 with very high overcast to 1.25 with a thick fog.

A procedure to detect clouds with the spectral radiometer was developed. One would prefer a procedure which is not dependent on air temperature and water vapor content. The ratio $E_n(\theta)$ is defined as the ratio of the radiance measured with filter n in the direction (zenith

angle) θ , divided by the corresponding radiance in the direction $\theta=80^\circ$. It was chosen as the parameter to indicate clouds. Using the ratio of radiances tends to eliminate the temperature sensitivity of the test. Using the radiance measured at a zenith angle of 80 degrees as a normalizing factor gives similar results to the use of the corresponding blackbody radiance referred to air temperature; however it is less sensitive to water vapor.

For the month of July, 1979 at Tucson, frequency distributions of $E_n(\theta)$ are shown in Fig. 11, for the filter channels in the atmospheric window. Each of these plots, has two local maxima. The maximum at the larger values of $E_n(\theta)$ corresponds to cloud observations while the other maximum represents clear skies. The points lying between the maxima correspond primarily to a cloud partially covering the radiometer's 2° field of view. Clouds are easier to detect overhead ($\theta = 0^\circ$) than near the horizon ($\theta = 60^\circ$), due to the smaller air mass through which the radiometer must view, as can be seen by the dotted lines in Fig. 11. In a similar manner, it is more difficult to detect clouds under conditions of high humidity than low humidity due to the increased absorption due to water vapor between the radiometer and the cloud.

The 8.8 micron filter is the least sensitive of the window filters to water vapor. Computations with our modified LOWTRAN 3B program [6] have been used to produce spectral radiance curves for clear atmospheric conditions for three values of water vapor concentration; these are displayed in Fig. 12. It can be seen that with 6 cm of precipitable water vapor, the 8.8 micron radiance has the most room for change when a cloud appears. As a test case, computed values of E_n were obtained

for 100% relative humidity and a surface temperature of 30°C. Table 1 gives values of $E_n(0^\circ)$ for clear skies and for a cloud layer at 4 km height. The 8.8 micron filter changed the most between clear and cloudy conditions. It was therefore chosen for the cloudy sky test.

Several of the measured clear sky maxima are plotted against dewpoint temperature in Fig. 13 to obtain correlations with dewpoint. An offset of 0.14 from the clear sky maxima of $E_n(\theta)$ was chosen to represent the division point between the clear and cloudy regimes. The precise value of this offset is somewhat arbitrary but we have verified that our final results are not substantially affected if other reasonable choices are made.

The correlations that were used for the 8.8 micron cloudy detection test as detection thresholds are as follows:

$$E_n(60^\circ) = (0.0060T_{dp} + 0.57) + 0.14 \quad (10a)$$

$$E_n(40^\circ) = (0.0079T_{dp} + 0.42) + 0.14 \quad (10b)$$

$$E_n(20^\circ) = (0.0072T_{dp} + 0.38) + 0.14 \quad (10c)$$

$$E_n(0^\circ) = (0.0070T_{dp} + 0.36) + 0.14. \quad (10d)$$

The clear sky values for E_n are given by the expressions in parentheses. Values of E_n greater than those specified by (10a-d) are identified with a cloud in the radiometer field of view.

The test for clouds is based only on the frequency distributions of the 8.8 micron filter radiance normalized by the simultaneous 80° radiance, and measurement of the dewpoint temperature. In order to obtain a more complete picture as to the strengths and weaknesses of this test we have used the LOWTRAN 3B model to simulate the cloudy sky test. Clouds were modeled as translucent grey-body emitters. For an ambient temperature of 30°C and a dewpoint of 16°C (relative humidity, 45%), which cloud types will be detected? Table 2 gives computed values of $E_n(\theta)$ of the 8.8 micron filter for 1, 4, and 12 km clouds of 0.25, 0.50, and 1.0 cloud (beam) emissivities. The test successfully detects opaque clouds (emissivity = 1) to an elevation of about 8 km, and detects translucent clouds (emissivity = 0.5) to about 4km. Low and middle clouds are normally very emissive, so that their detection is very probable. High level clouds will not be detected, but their effect on the sky radiation is minimal due to their low temperature. High clouds are also less

emissive than low clouds, which also reduces their effect upon the ground level radiance. Platt and Dilley report beam emissivities of 0.54 for cirrostratus [35], and cirrus emissivities should be even lower.

One limitation of the test for clouds is that it can only detect clouds between the zenith and 30 degrees above the north horizon. If the northern sky is clear but clouds are present the corresponding pyrgeometer observation is erroneously identified as obtained during clear conditions. In order to estimate the size of the errors in our final results caused by this effect we have examined the data for January, 1980 from Gaithersburg. A winter month was chosen for this test because the relative importance of clouds is greater during the winter. After a cloud was detected, data from the subsequent observation (30 minutes later) was also deleted, the inference being that there was a relatively large probability of an undetected cloud being present. Figure 14 shows the results for the (allegedly) clear sky emissivity versus dewpoint for a normal computer run compared with the run with probable clouds eliminated. The effect of undetected clouds upon our analysis appears to be quite small.

Pyrgeometer Calibration Procedure

A method for calibrating the pyrgeometer using the spectral radiometer was devised. Since the spectral radiometer is calibrated directly each day by a blackbody radiation source, the calibration of the pyrgeometer can be improved, or at least verified, if a calibration can be transferred to it from the spectral radiometer. Calibration adjust-

ments, or offsets, were obtained each month for the sky emissivity measurement. That is, the ratio $\epsilon_{\text{sky}} = S / (\sigma T_a^4)$ is used to represent the pyrgeometer measurements, and an offset generally in the range of 0 to 0.02 was applied to the measurements for the month. The offset is obtained in order to guarantee that if the pyrgeometer were exposed to blackbody radiation with a temperature equal to the air temperature, it will indicate a radiance of precisely σT_a^4 .

The measurements of the open hole channel (no filter) were used for the pyrgeometer calibrations. The spectral sensitivity of this channel is shown in Fig. 15. The radiances measured in the open hole channel were converted to emissivities by division with the radiance which would be measured if the sky were a blackbody with temperature T_a . (This radiance is computed for use with the spectral radiometers calibration procedure.) The open hole emissivities are then averaged over the sky dome, using the cosine of the zenith angle as a weighting function. The full-sky emissivity thus obtained will be termed the pseudo-pyrgeometer emissivity. It is quite similar to the pyrgeometer sky emissivity but the spectral weighting of different wavelengths is different (compare Fig. 10 and Fig. 15). Another difference is that the pseudo-pyrgeometer measurement pertains only to the northern portion of the sky. Nevertheless, there is a strong relationship between values of the actual and pseudo-pyrgeometer emissivities. Figure 16 shows a plot of the daily averages of the pseudo-pyrgeometer emissivity versus the measured pyrgeometer emissivity. The slope of this plot is related to the details of the spectral response of the two instruments involved. However, regardless of the slope of the line, it should pass through the point (1.0, 1.0), because this point represents blackbody radiation. Since the

spectral radiometer is calibrated by viewing a blackbody, the departure of the line of best fit from the point (1.0,1.0) is attributed to small errors in the pyrgeometer measurement. The calibration offset is thus the adjustment to the pyrgeometer emissivity necessary to intercept the point (1.0,1.0).

The actual procedure for obtaining the calibration offsets is somewhat more complex than just described, although it gives the same results to an accuracy of better than one percent. A procedure which utilizes all of the data points (rather than merely daily averages) was employed. Contour plots of the densities of data points are displayed in Figs.17-20. The closer the points come to (1.0,1.0), the more accurate the determination of the offset. Data with clouds present is included for this reason. Figure 20 shows a scatter plot where very few cloudy points occur (Tucson 9/79). This was the only month for which a reasonable offset was not obtainable.

A linear regression was initially attempted to fit a straight line through the data represented in Figs. 17-20. However, this procedure was inadequate. Least squares fits are the "best" fits when one has errors in the measured y coordinate and no errors in the x coordinate. In the case at hand there are errors in both x and y coordinates. A technique proposed by Acton[36] for such cases was used to obtain the offsets. The introduction of error on the x axis tends to spread out the x values and, in turn, flatten out the linear regression fit. When the points are grouped and averages used for the fit, the slope increases, because the random errors in the x coordinate tend to average out. Any noise which occurs in the y direction does not affect the

linear regression fit. Acton's technique requires the grouping of the individual points; a 24 hour period was used for this purpose. After grouping the points it is possible to estimate the "noise" in both the x and y directions and to adjust the linear fit to account approximately for the presence of the noise. For further detail of Acton's method consult reference 36. For the current purposes it is sufficient to observe that Acton's fitting procedure is effectively equivalent to the conceptually simpler linear regression through daily average values shown in Fig. 16.

A major flaw of the calibration procedure is that it is not possible to correct for the sun's effect upon the pyrgeometer. The sun causes a false pyrgeometer signal due to heating of the silicon dome, which indirectly heats the thermopile sensor. The sun also produces a small amount of radiation at wavelengths greater than 3 microns, which penetrates the silicon dome and is recorded as though it were atmospheric radiation. Although the calibration procedure uses both cloudy and clear data, the reference point (1.0,1.0) corresponds physically to the case of a very low overcast or fog. Thus the calibration procedure is not able to account for the effects of sunlight upon the pyrgeometer.

Pyrgeometer Error Analysis

A complete error analysis of the Eppley Pyrgeometer is well beyond the scope of the present paper. However, several of the most important causes of measurement uncertainty will be discussed. Issues which will not be discussed here include changes of the dome transmittance due to dust or temperature changes, deviations from the ideal cosine response

law, and deviations caused by the spectral dependence of the instrument's sensitivity. Each of these causes of measurement uncertainty is believed to be less important for our measurements than those discussed below.

A major portion of the instrument's output signal represents a correction for the thermal radiation leaving the instrument. This portion of the signal is proportional to σT^4 , where T is the absolute temperature of the instrument. The circuit producing this portion of the output signal contains several circuit elements energized with a small battery. Due to several non-ideal characteristics of this circuit it can lead to errors of roughly 0.02 in the measured sky emissivity. In our experiments the monthly average of this effect is reduced to zero by the procedure of obtaining calibration offsets from the spectral radiometer. However, when the highest precision is desired, the user should measure the pyrgeometer temperature directly (a thermistor is provided for this purpose) and compute the quantity σT^4 digitally rather than relying on the computation by an analog circuit. This procedure also avoids the possibility of data loss due to battery failure.

Probably the most significant errors for daytime measurements of sky emissivity are due to the solar heating of the dome. An earlier version of the Eppley pyrgeometer employed a KRS-5 (thallium bromide iodide) dome with an interference filter. The effect upon the instrument of the solar heating of the dome of this instrument was studied by Eng, Klink, and Baker[37]. They observed a solar effect of 20 to 120 Wm^{-2} in a sun and shade experiment, an effect they were able to reduce by ventilating the instrument. An experiment performed on the newer

pyrgeometer shows a similar but smaller effect. Table 3 displays data obtained in July, 1980 in Berkeley during a series of sun and shade experiments. These observations, made within two hours of solar noon during two periods of moderate to low wind speed, show a solar effect ranging from 20 to 30 Wm^{-2} . Also measured was the temperature to which the dome rose with respect to the base temperature when exposed to the sun. This temperature change occurs in synchronism with the change in pyrgeometer output. During the fourth trial a fan was used to increase the effective wind speed. This reduced the solar-induced temperature rise of the dome and the corresponding effect upon the pyrgeometer output. Also included in Table 3 is the $1/e$ time constant of the dome's temperature change (average of time to increase and time to decrease of the temperature). Since the instrument's time constant was independently measured to be about 5 seconds, the observed time constants reinforce the interpretation that the primary solar heating effect is not due to direct radiative transfer through the dome, but is in fact due to indirect heat transfer. Based on Table 3, we conclude that the response of the instrument due to a temperature increase of the dome is about 11 $\text{Wm}^{-2}\text{C}^{-1}$. Our calculated estimates of the heat transferred from the dome to the sensor due to such a temperature difference indicate an effect on the pyrgeometer output of about 12 $\text{Wm}^{-2}\text{C}^{-1}$. Three fourths of this effect is due to conduction within the air space between dome and sensor, and the other one fourth is due to infrared transfer. The overall effect of solar flux upon the instrument indicates that the pyrgeometer will read about 30 Wm^{-2} too high on a clear day with the sun overhead. The precise value of this error will depend on windspeed, with larger errors associated with lower windspeeds. In fact continuous

measurements made on a gusty clear day show signal variations of 10 Wm^{-2} or more as the fluctuating wind causes the dome temperature to vary, consistent with the variation shown in Table 3.

Another effect of solar radiation upon the pyrgeometer is transmission of radiation through the filtered dome. The transmission spectrum of the pyrgeometer dome is shown in Fig. 10. The transmittance of the dome rises to 50% of its maximum value at about 3.5 microns. A simple estimate of the solar transmission effect may be obtained by assuming the atmosphere is perfectly transmissive between 3.5 and 4.0 microns, and between 8 and 13 microns. The region 3.5 to 4.0 microns contains about 0.44% of the solar constant, while the region 8 to 13 microns contains about 0.09%[38]. Thus the pyrgeometer output should be increased by approximately 7 Wm^{-2} when the sun is overhead. An attempt was made to measure the magnitude of this effect directly with a sun and shade experiment using a thick (1.3 cm) piece of glass (Corning 7740). Glass in these thicknesses is opaque beyond 3.5 microns. In the sun and shade experiment, there should be an effect due to solar heating of the dome which is 15% of the effect using an opaque shade. There should also be an effect due to the absorption by the glass of wavelengths greater than 3.5 microns. These two effects can be distinguished from one another because the direct effect should occur with a time constant of 5 seconds or less, and the heating effect should occur with a time constant of 15 seconds or more. The experiment showed a direct transmission effect of less than 4 Wm^{-2} , consistent with zero. Thus the experiment was inconsistent with the theoretical estimate of 7 Wm^{-2} . Further experimentation is indicated to locate the source of the discrepancy; however it seems clear that the direct transmission effect is substantially

smaller than the effect due to the heating of the dome. In the absence of additional information, the rough theoretical estimate of 7 Wm^{-2} will serve as an estimate of the magnitude of the direct transmission effect when the sun is overhead on a clear day.

6. EXPERIMENTAL RESULTS

Calibration correction offsets were determined for daytime and nighttime data separately, for each month of data. After adding these correction offsets to the sky emissivity observations, least squares fitting was performed with the data to produce relationships between sky emissivity and dewpoint temperature. The results are shown in Tables 4 and 5, and in Figs. 21 and 22. Separate offsets for the daytime and the nighttime are presented because of the sun's effect on the daytime data. The calibration procedure should work well for the nighttime data, but is only partially effective for the daytime data, because the calibration is most accurate for periods of cloud cover when the solar effects on the pyrgeometer are minimized. The overall correlations are based on a linear regression with all the data points, excluding the month of September at Tucson, which did not include enough data points with clouds to produce a valid calibration. The nighttime correlation is

$$\epsilon_{\text{sky}} = 0.741 + 0.0062 T_{\text{dp}}, \quad (\text{night}) \quad (11)$$

where T_{dp} is the dewpoint temperature ($^{\circ}\text{C}$), based on 2945 individual measurements. The standard error of estimate for ϵ_{sky} is 0.031, representing the root mean square departure of the measurements from eqn.(11). This error in the estimation of ϵ_{sky} is partly due to measurement error and partly due to the various temperature and humidity profiles above the site for a given surface dewpoint temperature. We attribute the larger values of standard error for Gaithersburg to amplifier noise which was not present at the other sites. A fit to a quadratic function of T_{dp} reduced the standard estimate of error by less than 0.001, showing that a linear function of T_{dp} is adequate to

describe the data. The daytime correlation for the sky emissivity is

$$\epsilon_{\text{sky}} = 0.754 + 0.0058 T_{\text{dp}}, \quad (\text{uncorrected}) \quad (12)$$

based on 2896 individual measurements. The standard error of estimate is 0.033. This expression for the emissivity of the daytime sky is uncorrected for the effects of solar radiation upon the pyrgeometer. The range of dewpoint temperatures over which the emissivity relationships are valid is roughly -20°C to $+22^{\circ}\text{C}$. The average dewpoint temperature was 10°C , reflecting the fact that most of the data was obtained during the summer periods of higher dewpoint temperatures.

An interesting feature of the data is that there is no clear trend for one site or another to have higher or lower sky emissivities for the same values of dewpoint. Thus the relationship given by (11) may be sufficiently general to apply at locations other than the three shown in this study.

Due to the previously mentioned fact that the effect of sunlight upon the pyrgeometer raises doubts on the validity of the daytime result (12), a further investigation was made into the day/night differences of sky emissivity using the spectral radiometer. From the calibration curves for the pyrgeometer, an approximate correspondence is known between the psuedo-pyrgeometer and the pyrgeometer. The psuedo-pyrgeometer is based on the open filter of the spectral radiometer which views only the northern portion of the sky and is therefore quite solar blind due to its insensitivity to scattered solar radiation (see Fig.15). Using the psuedo-pyrgeometer, then, it is possible to measure the day/night difference in the thermal sky emissivity. Table 6 displays estimates of the day/night differences. The third column shows the

day/night difference in the sky emissivity as seen through the open hole filter at a zenith angle of 60° . This emissivity is roughly equal to the pseudo-pyrgeometer emissivity. The values were obtained by computing emissivity versus dewpoint correlations separately for day and night, and evaluating the difference between these relationships for the average dewpoint temperature. Note that the difference is always negative; that is, that the daytime sky is less emissive than the nighttime sky. This behavior is related to the formation of inversion layers during clear nights. The surface temperature is reduced compared with the temperature aloft. Thus the sky radiance is reduced by less than the change in σT_a^4 , where T_a is the air temperature, and consequently the sky emissivity is greater at night. The fourth column in Table 6 is the ratio of changes in the pseudo-pyrgeometer emissivity to changes in the pyrgeometer emissivity obtained from the calibration procedure. The final column in Table 6, the ratio of the two preceding columns, is the estimate of the day/night difference between the day and night emissivity versus dewpoint relationships. For clear skies, one can expect a day/night difference in the sky emissivity ranging from -0.010 to -0.023. The average value of this difference is -0.016. A least squares fit to the data listed in Table 6 yields the day/night emissivity difference for clear skies in the form

$$\Delta \epsilon_{\text{sky}} = -0.014 - 0.0002 T_{\text{dp}}.$$

The coefficient of T_{dp} in this equation is not significantly different from zero. Based on the nighttime relation, Eqn.(11), the sky emissivity due to the thermal atmospheric radiance alone is:

$$\epsilon_{\text{sky}} = 0.727 + 0.0060 T_{\text{dp}}. \quad (\text{day}) \quad (13)$$

The difference between (12) and (13) is due to the effect of solar radiation upon the pyrgeometer. (A portion of the solar effect may have been eliminated by the calibration procedure. Examine the difference in offsets between Tables 4 and 5.) Part of the difference between (12) and (13) is due to the direct transmission of the solar radiation through the filtered silicon dome. The other part is due to the solar heating of the dome, causing an apparent increase in the sky radiance. The size of the difference is consistent with the previous discussion of the effects of solar radiation upon the pyrgeometer.

7. COMPARISON WITH SELECTED EXPERIMENTAL AND THEORETICAL RELATIONS

The correlation of sky emissivity versus dewpoint for nighttime measurements is compared with the results of others in Fig. 23. Each empirical curve is extended over roughly the dewpoint range present in each experimenter's data. The curve ascribed to Sellers[13] is the median curve based on the results of a number of studies. The recent measurements of Clark and Allen[22] agree with our measurements for dewpoint temperatures above 0°C, but disagree at low dewpoints. The disagreement exceeds the estimated systematic error of approximately 0.03 thought to be present in each measurement set. This may indicate that San Antonio (where Clark and Allen's data were obtained) has more emissive skies in the winter than Gaithersburg (where our data at low dewpoint temperatures were obtained). All of the other measurements shown appear to be consistent with our own, even when no allowance is made for site-to-site differences.

The daytime and nighttime correlations of clear sky emissivity with dewpoint temperature are compared with several theoretical estimates in

Fig. 24. Each theoretical estimate of sky emissivity required assumptions for the "typical" profiles of temperature and humidity in the atmosphere. For our LOWTRAN estimates, the six model atmospheres present in the computer model were employed[25], together with the urban aerosol model with a visibility of 23 km. The LOWTRAN model is in striking, and possibly fortuitous, agreement with the measurements for each atmosphere except for the subarctic winter atmosphere. The relatively large emissivity computed in this case is evidently caused by the strong temperature inversion present in the subarctic winter temperature profile. The results of Bliss are in disagreement with our measurements. Bliss emphasized[31] that the values he used for the emissivity of water vapor were open to question, and in the face of contradictory evidence, chose values which now appear to be too large. Thus the disagreement with the measurements can be understood. The curve given by Staley and Jurica lies closer to the measurements, but still above them except at the highest dewpoint temperatures. No definite conclusion can be drawn in this case but the data do suggest that the values employed by Staley and Jurica for the emissivity of water vapor may be too large for water vapor amounts corresponding to surface dewpoint temperatures in the range of -10 to -20 °C.

8. APPLICATIONS OF THE EMISSIVITY RELATIONS

The Concept of Sky Temperature

The emissivity relations (11,13) provide useful estimates of sky radiance for computations of net heat loss to the sky. The equation

$$S = \epsilon_{\text{sky}} \sigma T_a^4 \quad (14)$$

is used to express the global thermal sky radiance S . For some applications it is preferred use the "sky temperature" T_{sky} instead of the sky emissivity. The sky temperature is defined by

$$S = \sigma T_{\text{sky}}^4. \quad (15)$$

The relationship between ϵ_{sky} and T_{sky} is

$$T_{\text{sky}} = \epsilon_{\text{sky}}^{1/4} T_a. \quad (16)$$

A horizontal grey-body radiating surface with emissivity ϵ_r produces a net radiative cooling rate N given by

$$N = \epsilon_r \sigma (T_r^4 - T_{\text{sky}}^4). \quad (17)$$

For most applications this equation can be accurately linearized in terms of $\Delta T = T_r - T_{\text{sky}}$:

$$N = h_r \Delta T, \quad (18)$$

where the radiative heat transfer coefficient h_r is equal to $4\epsilon_r T_r^3$. For a radiator temperature of 20°C (293°K) and $\epsilon_r = 1$, the coefficient h_r is $5.7 \text{ Wm}^{-2} \text{ }^\circ\text{K}^{-1}$ ($1.0 \text{ Btu ft}^{-2} \text{ hr}^{-1} \text{ }^\circ\text{F}^{-1}$ in English units). Thus the concept of a sky temperature permits the use of an analogy between radiative and conductive heat transport: the sky is regarded as having a temperature T_{sky} which is coupled to radiating surfaces with the "conduc-

tion" coefficient h_r .

Plots of the sky temperature depression, $T_a - T_{sky}$, versus dewpoint temperature for several air temperatures are shown in Fig. 25. This figure is based on the nighttime correlation (11) and eqn (16). The sky temperature depression --- the difference between the air temperature near the ground and the sky temperature --- is a convenient measure of the strength of the radiation cooling effect. For dewpoint temperatures below 0°C , such as occur during the winter at midlatitudes and even during the summer at desert locations, the sky is typically 20°C to 30°C colder than the air on clear nights. The corresponding daytime temperature differences are even larger. For warm, humid, cloudless conditions (dewpoint = 20°C , T_a greater than 20°C), the sky temperature depression is about 10° .

Estimating the Effect of Cloud Cover

For many applications it is necessary to estimate the thermal sky radiance in the presence of clouds. For this reason we present and discuss a simple method for accounting for clouds.

Let us denote the cloud cover by means of a superscript n which can range from 0 for clear skies to 1.0 for complete overcast. Thus the symbol ϵ_{sky} , used so far to represent the clear sky emissivity is modified to read $\epsilon_{sky}^{(0)}$, and the emissivity of generally cloudy skies is denoted $\epsilon_{sky}^{(n)}$. There are two commonly used formulae for computing the cloudy sky emissivity from the clear sky emissivity and cloud cover factors:

$$(1 - \epsilon_{\text{sky}}^{(n)}) = (1 - \epsilon_{\text{sky}}^{(0)}) C_n \quad (19)$$

and

$$\epsilon_{\text{sky}}^{(n)} = \epsilon_{\text{sky}}^{(0)} C_n' \quad (20)$$

The cloud cover factors C_n and C_n' are to be determined as functions of cloud amount n and cloud type. The factor C_n essentially transforms the cooling rate of a horizontal black surface at air temperature, while the factor C_n' transforms the sky radiation itself. It can be shown directly from eqns(19,20) that an error of, say, 0.1 in either C_1 or C_1' leads to the same size error in $\epsilon_{\text{sky}}^{(n)}$. There is no obvious reason to choose one form for the transformation over the other. One advantage of equation (19) is that for low thick clouds the factor C_n will approach 0, which requires the sky emissivity to approach unity, as it must. According to equation (20), for low thick clouds the factor C_n' must approach the inverse of the clear sky emissivity, and this is not generally possible if the cloud cover factor is to be independent of non-cloud parameters.

To better answer the question of which cloud cover parameter is to be preferred, a simple numerical experiment was performed with our LOWTRAN computer model. Opaque cloud layers were simulated at heights of 1, 4, and 10 kilometers. The layers were treated simply as black bodies, with the temperature of the atmosphere at the corresponding levels. (The assumption that the 10 km. cloud is opaque is not strictly accurate since cirrus clouds have emissivities less than unity[35]). Values of sky emissivity with and without each cloud were computed and values of C_1 and C_1' were derived from eqns.(19,20). These values are plotted in Fig. 26 for four of the LOWTRAN model atmospheres. It is

apparent from the figure that C_1' shows more variation than C_1 for the differing profiles of atmospheric temperature and humidity in these model atmospheres. For high clouds both cloud cover factors show about the same amount of spread, but for medium and low clouds the factor C_n is preferred. Thus, although the evidence is primarily circumstantial, we favor the use of the cloud cover factor C_n to account for the presence of clouds.

It remains to discuss the dependence of the cloud cover factor C_n on cloud cover amount n and upon cloud type. Fig. (26) shows estimates of the factor C_1 made by Sellers[13], plotted as discrete points. Each point represents a specific cloud type. It would appear that the cloud cover factor is primarily a function of cloud height (or cloud base temperature) for complete overcast.

For partial overcast, a simple linear interpolation of the cloud cover factor based on the fraction of cloud cover seems justified[18,22]. It would appear that the limitations of both the visual observations of cloud cover and the available accuracy of measured sky radiances make a non-linear interpolation formula of questionable value. Therefore, the cloud cover factor has the form

$$C_n = 1 - \Gamma n \quad (21)$$

where Γ is a parameter determined by the cloud type. It is small for high clouds and approaches unity for low clouds. Based on Seller's estimates (shown in Fig.(26)) values for Γ are 0.16 for cirrus (height 12.2 km.), 0.66 for altocumulus (height 3.7 km.), and 0.88 for stratocumulus (height 1.2 km.). Exell[33] has presented a formula for application to the case in which several cloud types are present

simultaneously. For average cloud cover conditions it is desirable to use the average opaque cloud cover measurement (regarding cirrus clouds as a clear sky) in order to obtain average values of the cloud cover factor. Based on measurements made by Picha and Villanueva[18] at Atlanta and by Clark and Allen at San Antonio[22], the average value of Γ can be estimated as 0.6 and 0.56, respectively, at these locations. However, even for average conditions, the parameter Γ probably varies with geographic location and season.

In summary, to modify our results (11,13) for the emissivity of clear skies to account for the average presence of clouds, one may use the formula based on (19,21):

$$\epsilon_{\text{sky}}^{(n)} = \epsilon_{\text{sky}}^{(0)} (1 - \Gamma n) + \Gamma n, \quad (22)$$

where n is the fraction of opaque cloud cover and Γ is a parameter equal to approximately 0.6.

Estimating the Spectral Distribution of Thermal Sky Radiation

It is not difficult to provide reliable estimates for the amount of thermal radiation within the 8 to 13 micron atmospheric window, based on the total sky emissivity ϵ_{sky} and the absolute air temperature T_a . The reason such estimates can be made is that the atmospheric emission outside the window is to a good approximation equal to that of a black body at air temperature, as discussed in Section 2. Let S_w be the portion of total thermal sky radiance S which falls within the window region:

$$S_w = \int_{\lambda_1}^{\lambda_2} d\lambda \int d\Omega \cos\theta R(\lambda, \theta), \quad (23)$$

where $R(\lambda, \theta)$ is the spectral radiance of the sky per unit wavelength and

solid angle (Ω). The limits of integration λ_1 and λ_2 represent the boundaries of the atmospheric window. For dewpoint temperatures above about 0°C , the limits $\lambda_1 = 8 \mu\text{m}$, $\lambda_2 = 13 \mu\text{m}$ are appropriate. Let f_w be the fraction of blackbody radiance which falls within the atmospheric window:

$$f_w = \int_{\lambda_1}^{\lambda_2} d\lambda B(\lambda, T_a) / \int_0^{\infty} d\lambda B(\lambda, T_a), \quad (24)$$

where $B(\lambda, T_a)$ is the Planck function evaluated with the absolute air temperature T_a . The fraction f_w can be estimated with Fig.1 although accuracy is difficult to obtain.† The assumption that $R(\lambda, \theta) = B(\lambda, T_a)$ for λ outside the atmospheric window can now be used to show from (23) and (24) that

$$S = S_w + (1-f_w)\sigma T_a^4.$$

Since S has the form $\epsilon_{\text{sky}}\sigma T_a^4$, the window thermal sky radiance is

$$S_w = [\epsilon_{\text{sky}} - (1-f_w)] \sigma T_a^4. \quad (25)$$

This formula can be used with estimates of sky emissivity and air temperature to provide performance estimates for selective radiative cooling devices.

9. SUMMARY

The thermal radiation from clear skies has been measured at three locations in the southern United States. Relations for nighttime and daytime estimates of the emissivity of clear skies have been presented to summarize the data. Only the surface dewpoint temperature is

† For $\theta_1 = 8 \mu\text{m}$, $\theta_2 = 13 \mu\text{m}$ and $T_a = 260, 290, 320^\circ\text{K}$, f_w has the values 0.277, 0.313, and 0.335.

required to produce an estimate of the clear sky emissivity. One relation for nighttime measurements and one for daytime measurements fit the summertime data for three cities. These same relations also fit the data for wintertime measurements at Gaithersburg, Maryland.

The diurnal variation of clear sky emissivity is small and is caused primarily by the development of nighttime temperature inversions. Based on our measurements for clear skies the average daytime sky emissivity is 0.016 smaller than the average nighttime sky emissivity.

Our results can be applied to compute the heat transfer by thermal radiation from surfaces exposed to the sky. Solar energy applications of particular interest are performance calculations for radiative cooling systems, calculations of heat loss from solar collector glazings, and building energy analysis computations of the heat loss or gain at exterior surfaces.

10. ACKNOWLEDGEMENTS

Marlo Martin played a major role in the guidance of this project and in the early design of the spectral radiometer instrumentation system. He also made the key suggestion that it was possible to transfer calibrations from the spectral radiometer to the pyrgeometer. The spectral radiometer instrumentation system was designed and constructed by our Laboratory's Special Projects Group. Jerry Stoker of this group supervised equipment construction and was primarily responsible for the continued operation of the equipment. Peter Fuller had the responsibility for interrogating the remote systems to transfer the data to our laboratory.

The cooperating individuals at the remote sites and their institutions were Paul Carlson, Kitt Peak National Observatory (Tucson); John Jenkins, National Bureau of Standards (Gaithersburg); and Albert J. Pallmann, St. Louis University.

We also acknowledge useful conversations regarding the Eppley pyrgeometer with Walter Scholes, Eppley Laboratory; Chuck Miller, Energy Alternatives Incorporated; and Gene Clark, Trinity University.

This work was supported by the Assistant Secretary for Conservation and Renewable Energy, Office of Solar Applications for Buildings, Passive and Hybrid Division of the U.S. Department of Energy under Contract No. W-7405-ENG-48.

11. REFERENCES

1. F. Trombe, Perspectives sur l'utilisation des rayonnements solaires et terrestres dans certains regions du monde, Rev. Generale de Thermique 6, 1285, (1967).
2. A.K. Head, Australian patent 239364 (1959); Method and Means for Producing Refrigeration by Selective Radiation ,U.S. patent 3043112 (1962).
3. S. Catalanotti, V. Cuomo, G. Piro, D. Ruggi, V. Silvestrini and G. Troise, The Radiative Cooling of Selective Surfaces, Solar Energy 17, 83 (1975).
4. A. Addeo, E. Monza, M. Peraldo, B. Bartoli, B. Coluzzi, V. Silvestrini and G. Troise, Selective Covers for Natural Cooling Devices, Nuovo Cimento 1C, 419 (1978).
5. R.A. McClatchey, R.W. Fenn, J.E.A. Selby, F.E. Voltz and J.S. Garing, Optical Properties of the Atmosphere. third ed., U.S. Air Force Cambridge Research Laboratory, Bedford, Massachusetts, AFCRL-72-0497 (1972). Available from the National Technical Information Service, U.S. Dept. of Commerce, Springfield VA 22151.
6. P. Berdahl and M. Martin, The Resource for Radiative Cooling, Proc. of the Third National Passive Solar Conf., Vol. 2, 684 (Philadelphia, 1978).
7. K. Bignell, F. Saeedy, and P.A. Sheppard, On the Atmospheric Infrared Continuum, J. of the Optical Soc. of Amer. 54, 466 (1963).
8. Ref. 7. Also see Ref. 27, p.57.
9. H.R. Carlon and C.S. Harden, Mass Spectrometry of Ion-induced Water Clusters: An Explanation of the Infrared Continuum Absorption, Appl. Opt. 19, 1776 (1980).

10. R. Geiger, The Climate Near the Ground, Havard University Press, Cambridge (1959). Translated from the second German edition by M.N. Stewart.
11. K. Ya. Kondratyev, Radiative Heat Exchange in the Atmosphere, Pergamon Press, New York (1965). Translated from the Russian by O. Tedder.
12. K. Ya. Kondratyev, Radiation in the Atmosphere, Academic Press, New York (1969).
13. W.D. Sellers, Physical Climatology, Univ. of Chicago Press, Chicago (1965).
14. A. Anstrom, Uber die Gegenstrahlung der Atmosphere, Meteorol. Z. 33, 529 (1916).
15. D. Brunt, Notes on Radiation in the Atmosphere, Quart. J. R. Meteor. Soc. 58, 389 (1932).
16. D. Brunt, Radiation in the Atmosphere, Quart. J. R. Meteor. Soc. 66 (Suppl.), 34 (1940). This paper corrects an error in Ref.15.
17. W.H. Dines and L.H.G. Dines, Monthly Mean Values of Radiation from Various Parts of the Sky at Benson, Oxfordshire, Mem. R. Meteor. Soc. 2, 1 (1927).
18. K.G. Picha and J. Villanueva, Noctunal Radiation Measurements, Atlanta, Georgia, Solar Energy 6, 151 (1962).
19. J.R. Goss and F.A. Brooks, Constants for Empirical Expressions for Downcoming Atmospheric Radiation under Cloudless Sky, J. of Meteor. 13, 482 (1956).
20. J.L. Monteith, An Empirical Method for Estimating Long-wave Radiation Exchanges in the British Isles, Q.J. Roy. Meteor. Soc. 87, 171 (1961).

21. R.E. Roberts, J.E. Selby, and L.M. Biberman, Infrared Continuum Absorption by Atmospheric Water Vapor in the 8-12 Micron Window, Applied Optics 15, 2085 (1976).
22. G. Clark and C.P. Allen, The Estimation of Atmospheric Radiation for Clear and Cloudy Skies, Proc. of the Second National Passive Solar Conf., Vol. 2, 676 (Philadelphia, 1978).
23. W.C. Swinbank, Longwave Radiation from Clear Skies, Quart. J. Roy. Meteor. Soc. 89, 339 (1963). Also Vol.90, p. 488.
24. S.B. Idso and R.D. Jackson, Thermal Radiation from the Atmosphere, J. Geophys. Res. 74, 5397 (1969).
25. J.E.A. Selby, E.P. Shettle, and R.A. McClatchey, Atmospheric Transmittance from 0.25 to 28.5 Microns: Supplement LOWTRAN 3B, U.S. Air Force Geophysical Laboratory, Hanscom AFB, Massachusetts, AFGL-TR-76-0258 (1976). Available from NTIS (see Ref. 5).
26. J.E.A. Selby, F.X. Kneizys, J.H. Chetwynd Jr., and R.A. McClatchey, Atmospheric Transmittance/Radiance: Computer Code LOWTRAN 4, U.S. Air Force Geophysical Laboratory, Hanscom AFB, Massachusetts, AFGL-TR-78-0053 (1978). Available from NTIS (see Ref. 5).
27. F.X. Kneizys, E.P. Shettle, W.O. Gallery, J.H. Chetwynd Jr., L.W. Abreu, J.E.A. Selby, R.W. Fenn and R.A. McClatchey, Atmospheric Transmittance/Radiance: Computer Code LOWTRAN 5, U.S. Air Force Geophysical Laboratory, Hanscom AFB, Massachusetts, AFGL-TR-80-0067 (1980). Available from NTIS (see Ref. 5).
28. A. Ben-Shalom, B. Barzilai, D. Cabib, A.D. Devir, S.G. Lipson and U.P. Oppenheim, Sky Radiance at Wavelengths between 7 and 14 Microns; Measurement, Calculation, and Comparison with LOWTRAN 4 Predictions, Appl. Opt. 19, 838 (1980).

29. P. Berdahl and M. Martin, Spectral Radiance of the Clear Midlatitude-Summer Atmosphere, in Volume of Extended abstracts for the 1980 International Radiation Symposium, 167 (Fort Collins, Colorado, 1980).
30. W.L. Wolfe and G.J. Zissis, eds., The Infrared Handbook, Prepared by The Infrared Information and Analysis Center of the Environmental Research Institute of Michigan, Chap. 5 (1978).
31. R.A. Bliss, Atmospheric Radiation Near the Surface of the Ground: a Summary for Engineers, Solar Energy 5, 103 (1961).
32. M.A. Atwater and J.T. Ball, Computation of IR Sky Temperature and Comparison with Surface Temperature, Solar Energy 21, 211 (1978).
33. R.H.B. Exell, The Atmospheric Radiation Climate of Thailand, Solar Energy 21, 73 (1978).
34. D.O. Staley and G.M. Jurica, Effective Atmospheric Emissivity Under Clear Skies, J. Appl. Meteor. 11, 349 (1972).
35. C.M.R. Platt and A.C. Dilley, Remote Sounding of High Clouds: II. Emissivity of Cirrostratus, J. Appl. Meteor. 18, 1144 (1979).
36. F.S. Acton, Analysis of Straight-Line Data, John Wiley and Sons, Inc. New York, p.135 (1959).
37. J.W.ENZ, J.C. Klink, and D.G. Baker, Solar Radiation Effects on Pyrgeometer Performance, J. Appl. Meteor. 14, 1297 (1975).
38. K.L. Coulson, Solar and Terrestrial Radiation, Academic Press, New York (1975).

Table Headings

Table 1: Computed values of $E_n(0^\circ)$ for warm very humid conditions.

Table 2: $E_n(\theta)$ for the $8.8 \mu m$ filter (ratio of radiance at zenith angle θ to that at $\theta = 80^\circ$).

Table 3: Response when pyrgeometer is unshaded.

Table 4: Clear sky emissivity versus dewpoint correlations. Nighttime data only.

Table 5: Clear sky emissivity versus dewpoint correlations. Daytime data only. Data not corrected for effect of sunlight on pyrgeometer.

Table 6: Data used to obtain the average day/night difference in the emissivity of clear skies.

Table 1.

Relative Humidity	Condition	Filters			
		8-14 μ m	8.8 μ m	9.6 μ m	11.0 μ m
100%	clear	0.92	0.84	0.87	0.91
100%	cloudy	0.97	0.94	0.95	0.97

Zenith angle (θ)	E_n threshold	Cloud height: Cloud beam emissivity:	1 km			4 km			12 km		
			1.0	0.5	0.25	1.0	0.5	0.25	1.0	0.5	0.25
60°	0.81		.98	.87	.74	.88	.80	.71	.69	.67	.65
40°	0.69		.97	.75	.60	.84	.68	.57	.58	.54	.51
20°	0.63		.96	.68	.54	.83	.61	.51	.54	.48	.45
0°	0.62		.96	.66	.52	.82	.59	.49	.52	.46	.44

Table 2.

Table 3.

Trial	$T_{\text{dome}} - T_{\text{base}}$ (°C)	ΔS (Wm ⁻²)	t_c (sec)
1	2.3	28	34
2	2.3	28	27
3	3.0	31	29
4	2.2	21	17

Site	Month/Yr	Number of Observations	Average Dewpoint (°C)	Offset Correction $\Delta\epsilon$	Intercept $\epsilon_{\text{sky}}(^{\circ}\text{C})$	Slope $d\epsilon_{\text{sky}}/dT_{\text{dp}}$	Std. Error of Estimate
Gaithersburg	6/79	90	13	-0.036	0.690	0.0085	0.026
	7/79	247	16	-0.010	0.724	0.0083	0.041
	8/79	261	17	-0.010	0.716	0.0084	0.035
	9/79	343	13	-0.014	0.711	0.0081	0.050
	1/80	210	-9	+0.018	0.760	0.0068	0.031
	2/80	295	-14	0.000	0.755	0.0074	0.029
St. Louis	7/79	237	16	+0.007	0.720	0.0074	0.021
	8/79	313	20	+0.014	0.794	0.0031	0.017
Tucson	6/79	297	4	+0.017	0.747	0.0050	0.011
	7/79	354	10	+0.011	0.740	0.0059	0.013
	8/79	298	12	+0.018	0.716	0.0080	0.016
	9/79	386	8	+0.057	0.794	0.0052	0.020
All Data Except Tucson 9/79	-	2945	9.1	-	0.741	0.0062	0.031

Table 4.

Site	Month/Yr	Number of Observations	Average Dewpoint (°C)	Offset Correction ΔF	Intercept $\epsilon_{sky}(0^\circ\text{C})$	Slope $d\epsilon_{sky}/dT$	Std. Error of Estimate
Gaithersburg	6/79	90	12	-0.019	0.735	0.0079	0.057
	7/79	243	16	-0.021	0.724	0.0074	0.038
	8/79	279	18	-0.016	0.738	0.0067	0.037
	9/79	285	14	-0.011	0.749	0.0059	0.048
	1/80	95	-8	+0.018	0.759	0.0053	0.029
	2/80	251	-12	+0.008	0.766	0.0064	0.026
St. Louis	7/79	287	16	+0.004	0.747	0.0067	0.024
	8/79	324	20	+0.012	0.780	0.0046	0.020
Tucson	6/79	272	6	+0.004	0.746	0.0054	0.028
	7/79	415	12	+0.010	0.750	0.0056	0.024
	8/79	355	13	+0.017	0.716	0.0082	0.016
	9/79	345	10	+0.047	0.789	0.0048	0.022
All Data Except Tucson 9/79	-	2896	11.3	-	0.754	0.0058	0.0033

Table 5.

Site	Month/Yr	Dewpoint Temperature (°C)	$\Delta\epsilon_{60^\circ, \text{open}}$	Calibration ratio	Day/night difference $\Delta\epsilon_{\text{sky}}$
Gaithersburg	6/79	12	-0.016	1.2	-0.013
	7/79	16	-0.032	1.5	-0.021
	8/79	18	-0.036	1.6	-0.023
	9/79	14	-0.034	1.5	-0.023
	1/80	-8	-0.014	1.4	-0.010
	2/80	-13	-0.016	1.3	-0.012
St. Louis	7/79	16	-0.019	1.6	-0.012
	8/79	20	-0.018	1.6	-0.011
Tucson	6/79	5	-0.020	1.4	-0.014
	7/79	11	-0.018	1.4	-0.013
	8/79	12	-0.032	1.5	-0.021
	9/79	9	-0.023	1.8	-0.013

Table 6.

Figure Captions

Fig.1: Fraction of blackbody energy with wavelength less than λ^* . The horizontal axis is linear in $\ln(\lambda^*)$. The vertical axis is linear in $\ln[f/(1-f)]$, where f is the fraction in question. In these coordinates the curve is merely displaced to the right or left by changes of temperature. The 50% point of the spectrum for temperature T ($^{\circ}\text{K}$) occurs at a wavelength λ^* (μm) given by $\lambda^* T = 4110 \mu\text{m}^{\circ}\text{K}$.

Fig.2: Low resolution absorption spectra:

- (a) Absorption due to water vapor along a 10 km path with 1 gm/cm^2 water vapor.
- (b) Absorption due to carbon dioxide along a 5 km path at sea level.
- (c) Absorption due to 0.3 atm-cm of ozone.
- (d) Absorption from all atmospheric constituents for a path through the cloudless atmosphere.

Fig.3: Estimated spectral radiance of the cloudless sky for zenith angles of 0° , 60° , 75° , and 90° (horizon). Assumptions of "typical" summer conditions include surface air and dewpoint temperatures of 21°C and 16°C .

Fig.4: Estimated spectral radiance of the cloudless sky for zenith angles of 0° , 60° , 75° , and 90° . Assumptions of typical winter conditions include surface air and frostpoint tem-

peratures of -1°C and -5°C .

Fig.5: Estimated spectral radiance of the cloudy sky for zenith angles of 0° , 60° , 75° , and 90° . The atmospheric conditions are assumed to be identical to those for Fig.3, but a cloud layer has been added with a cloud base height of 4 km.

Fig.6: Blackbody radiant flux for temperatures in the environmental range compared with the corresponding flux for a clear atmosphere with air temperature near the ground of 294°K . The solid curve is a rough estimate of spectral radiant flux received from the entire sky dome. It was obtained by taking the 60° curve from Fig.3 and multiplying by w .

Fig.7: Energy balance of a horizontal blackbody emitter exposed to the sky. In this illustration, the blackbody emitter will warm up from 20°C below air temperature) because the energy absorbed area is greater than the energy emitted area.

Fig.8: A perfect selective emitting surface operating 10°C below air temperature should be emissive only from 8 to 13 microns. Emission outside the 8 to 13 micron window would necessitate absorption of the "warm" atmospheric radiation present outside the atmospheric window.

Fig.9: A perfect selective emitting surface operating 20°C below air temperature should be emissive only from 8 to 12.5 microns.

- Fig.10: Approximate spectral transmission of the silicon pyrgeometer dome.
- Fig.11: Frequency distributions of the parameters $E_n(\theta)$ used to detect the presence of clouds. For reasons of clarity the distributions for zenith angles of 20° and 40° are not shown. The small size of the peaks corresponding to cloudy conditions at high values of $E_n(\theta)$ reflects the infrequent appearance of clouds during July in Tucson.
- Fig.12: Spectral radiance of the zenith portion of the cloudless sky for differing amounts of atmospheric water vapor.
- Fig.13: Values of $E_n(\theta)$ for the 8.8 micron filter for clear skies as a function of average surface dewpoint temperature. Each point represents the maximum of a distribution of the type shown in Fig.11b. The solid lines represent the parametric fits of $E_n(\theta)$ as a function of dewpoint used in eqn.(10).
- Fig.14: Sensitivity of inferred correlation of clear sky emissivity versus dewpoint to a change in the cloud detection test. The usual test is based on 341 observations. The altered test is based on 313 observations, with apparently cloudless observations deleted if the prior observation detected clouds.

- Fig.15: The relative response of the spectral radiometer with the open hole "filter". The response is primarily determined by the coated germanium lens.
- Fig.16: Illustration of the determination of the offset correction for the pyrgeometer. Each point is based on the daily average pyrgeometer and pseudo-pyrgeometer emissivities. Data with clouds present is included.
- Fig.17: Contours delineating the density of joint observations of pseudo-pyrgeometer and pyrgeometer. The inner contour represents 8 times the density of the outer contour. Sept. 1979 at Gaithersburg.
- Fig.18: Density contours as in Fig.17, for July 1979 at Tucson.
- Fig.19: Density contours as in Fig.17, for July 1979 at St. Louis.
- Fig.20: Density contours as in Fig.17, for Sept. 1979 at Tucson. In this case the data points do not approach the point (1.0,1.0) closely enough to provide an accurate calibration for the pyrgeometer.
- Fig.21: Nighttime correlations for clear sky emissivity versus dewpoint temperature. Each line segment represents a correlation based on 1 month of data at a given site, centered at the average dewpoint temperature for the relevant set of observations. The Gaithersburg observations are: 1 - June,

1979; 2 - July, 1979; 3 - August, 1979; 4 - Sept., 1979; 5 - Jan., 1980; 6 - Feb., 1980. The St. Louis observations are: 7 - July, 1979; 8 - August, 1979. The Tucson observations are: 9 - June, 1979; 10 - July, 1979; 11 - August, 1979. The continuous line is the correlation based on the 2945 individual data points.

Fig.22: Daytime correlations for clear sky emissivity versus dewpoint. See Fig.21 for identification of the data sets represented. The continuous line is the correlation based on the 2896 individual data points. This data is uncorrected for the effects of sunlight upon the pyrgeometer.

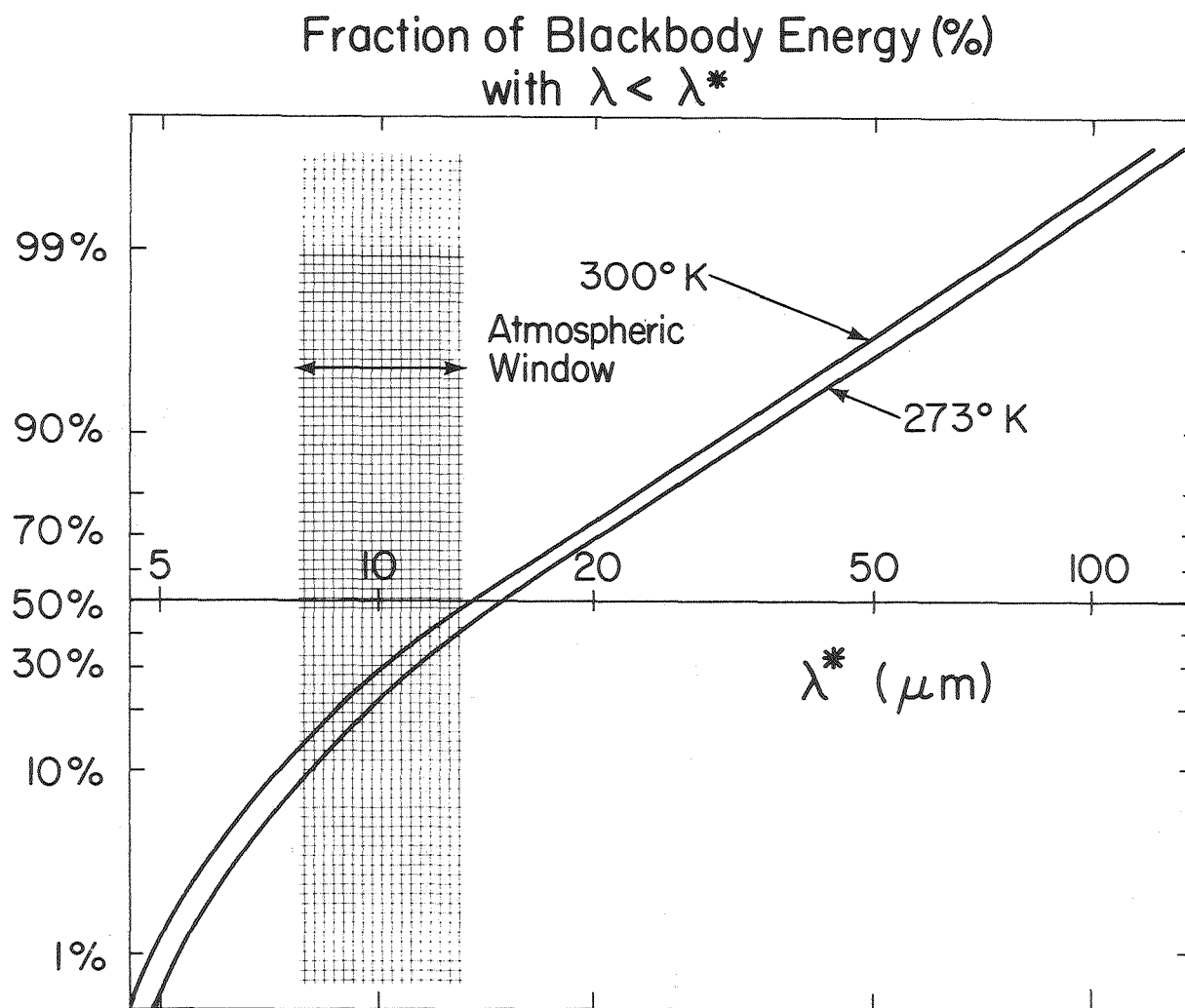
Fig.23: Comparison of our nighttime correlation (heavy line) with experimental results of others. The result ascribed to Sellers[13] is based on median parameters drawn from data published by a number of other authors. Each curve extends over the approximate range of dewpoint of the observations.

Fig.24: Comparison of our daytime and nighttime correlations with theoretical estimates. Each theoretical estimate incorporates (slightly different) estimates of temperature and humidity profiles above the point of observation. The LOWTRAN results (circles) are based on our calculations with LOWTRAN 3B using the 6 model atmospheres. The properties of these atmospheres are listed in several references

[25,26,27,30]. From left to right the LOWTRAN atmosphere names are Subarctic Winter, Midlatitude Winter, U.S. Standard, Subarctic Summer, Midlatitude Summer, and Tropical.

Fig.25: Sky temperature depression (air temperature minus sky temperature) as a function of dewpoint temperatures for clear nighttime sky conditions.

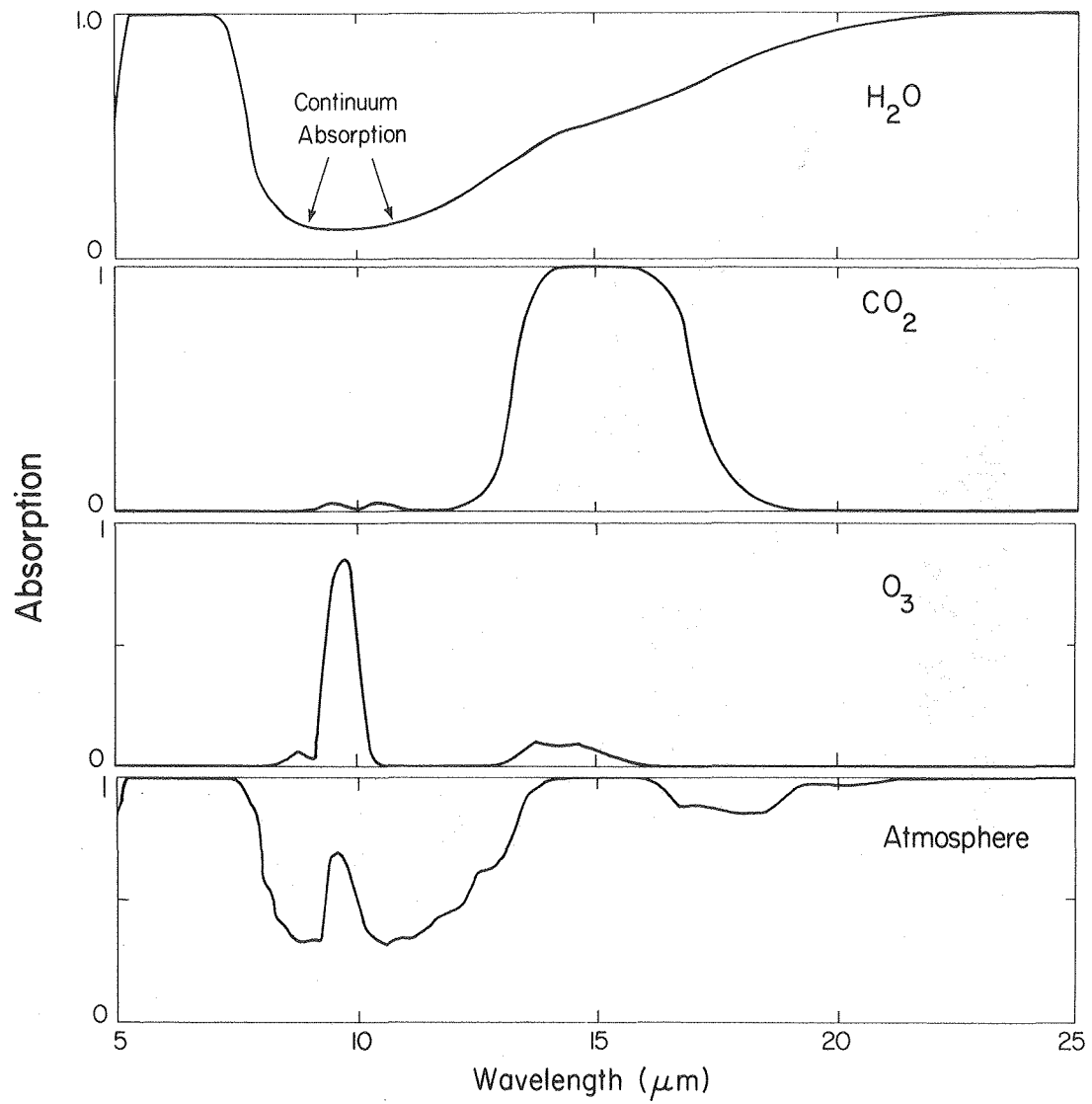
Fig.26: Computed cloud cover factors as a function of cloud height for four LOWTRAN model atmospheres. 1 - Tropical, 2 - Midlatitude Summer, 3 - Midlatitude Winter, 4 - U.S. Standard. The triangles on the graph for C_1 from Sellers[13].



XBL 813-517

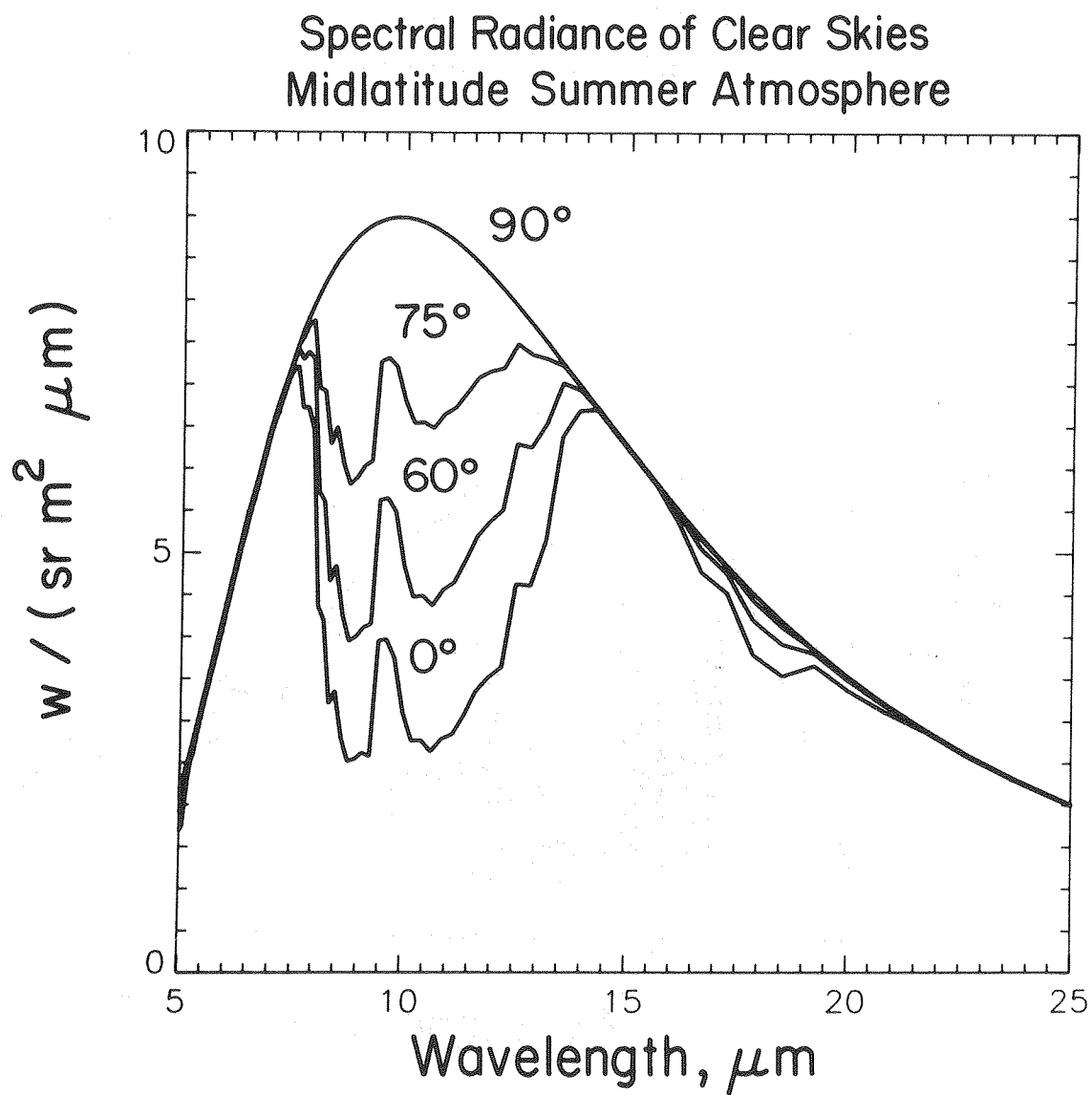
Figure 1.

Figure 2.



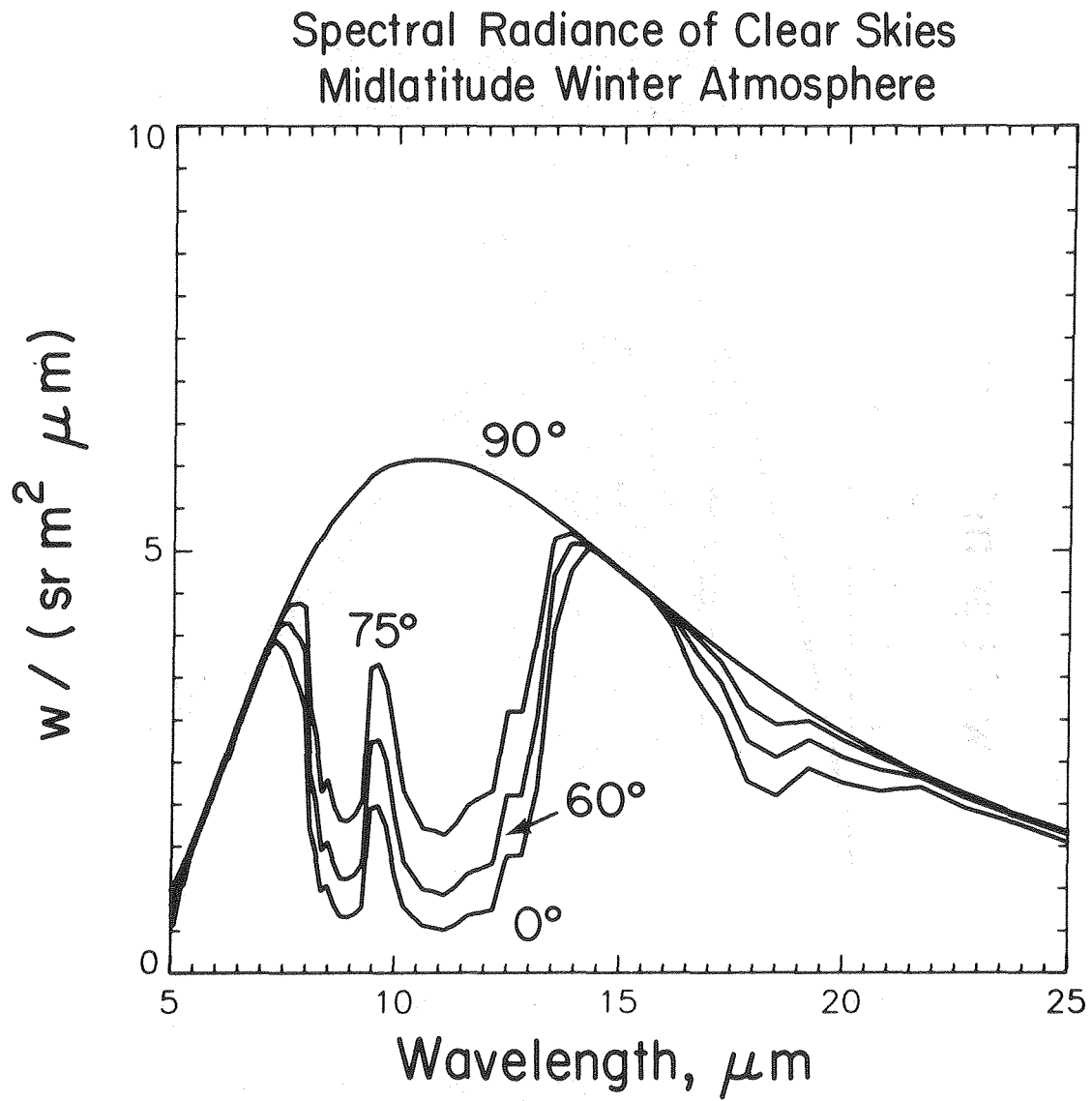
XBL 813-519

Figure 3,



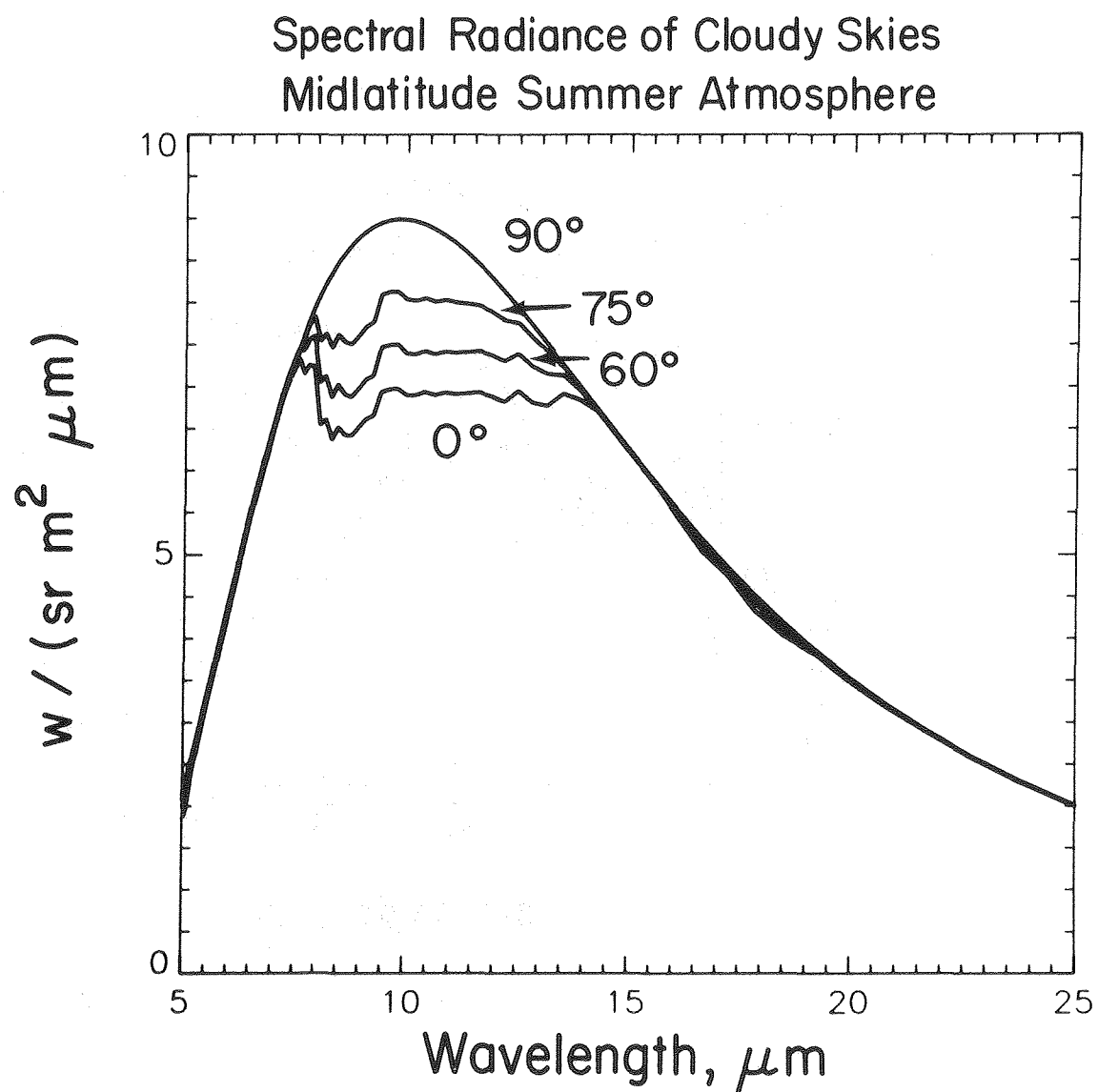
XBL 813-520

Figure 4.



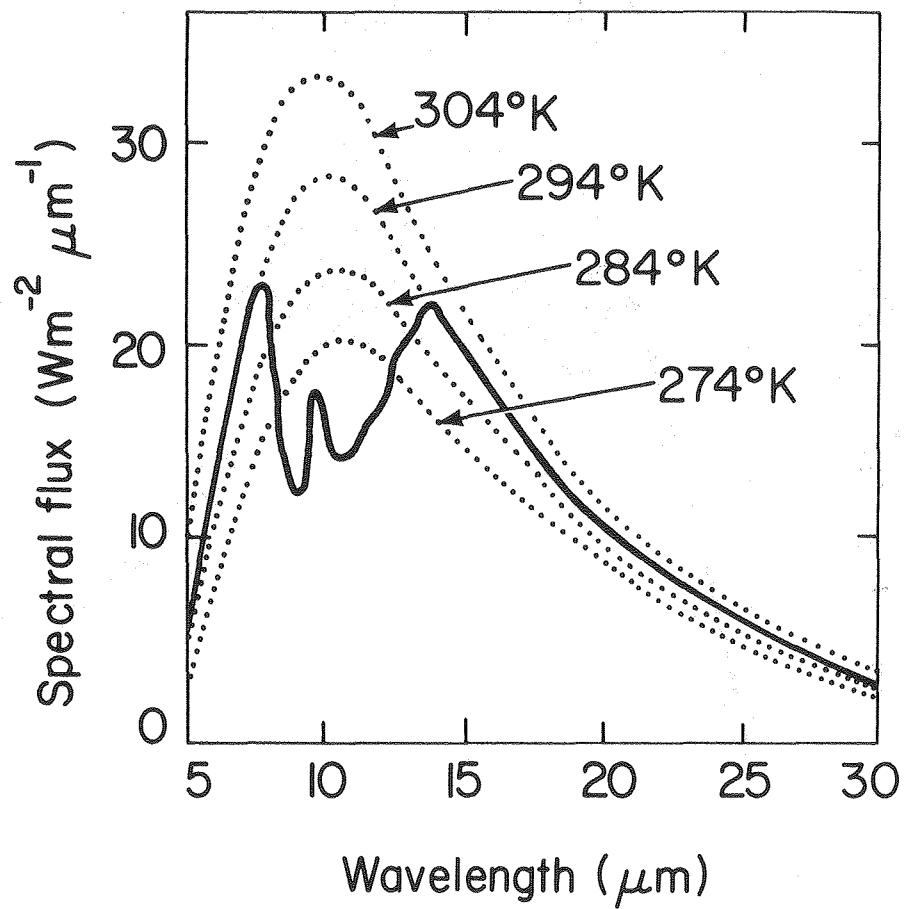
XBL 813-521

Figure 5.



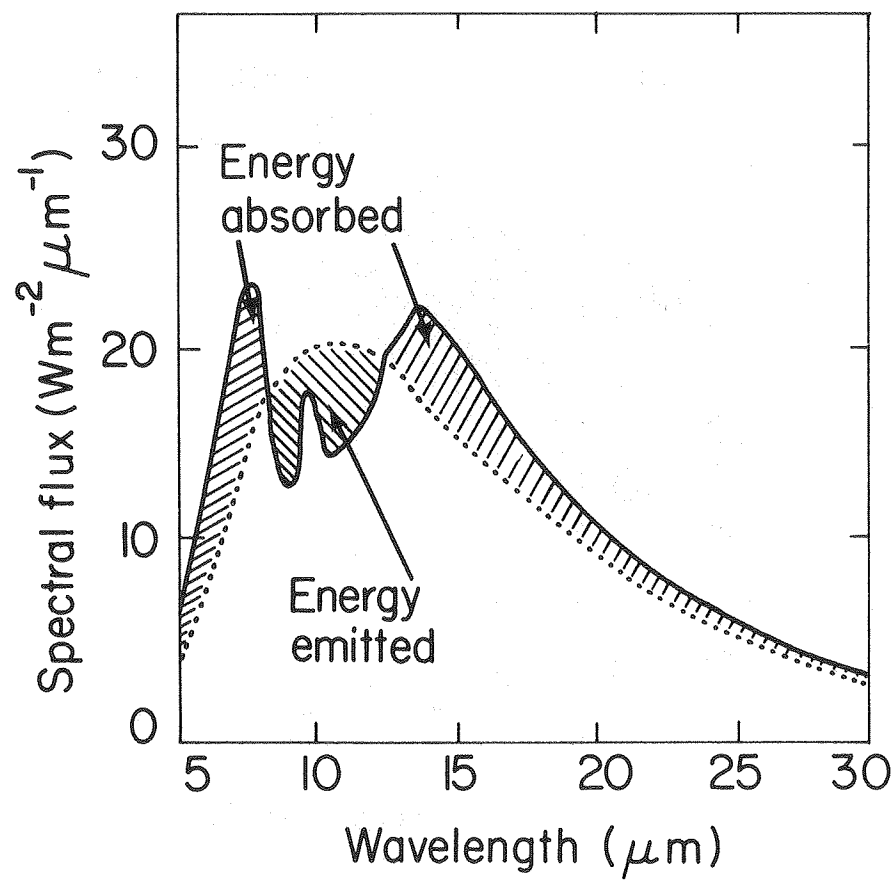
XBL 813-522

Figure 6.



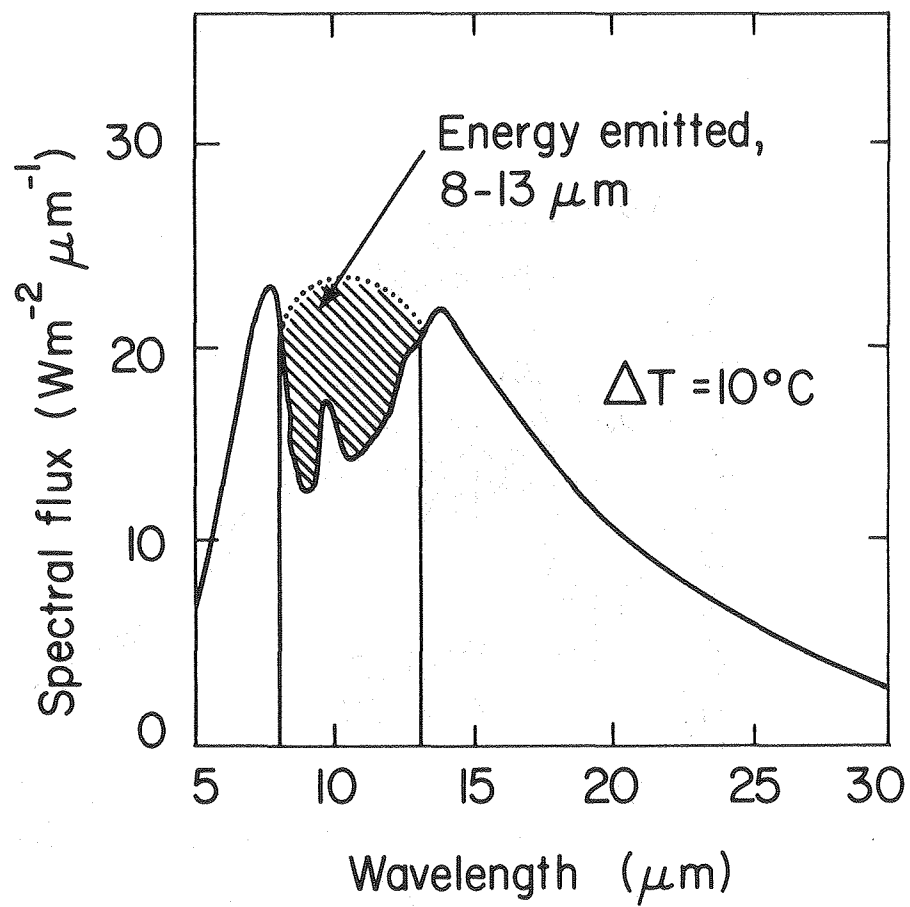
XBL 813-523

Figure 7.



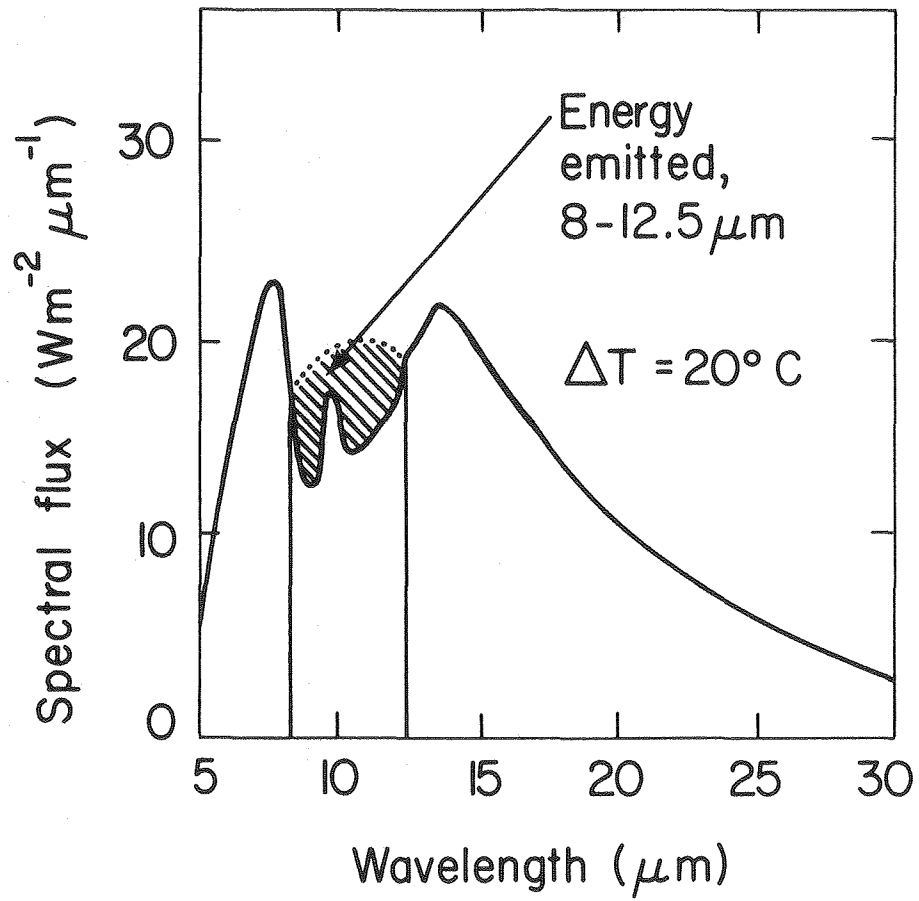
XBL 813-524

Figure 8.



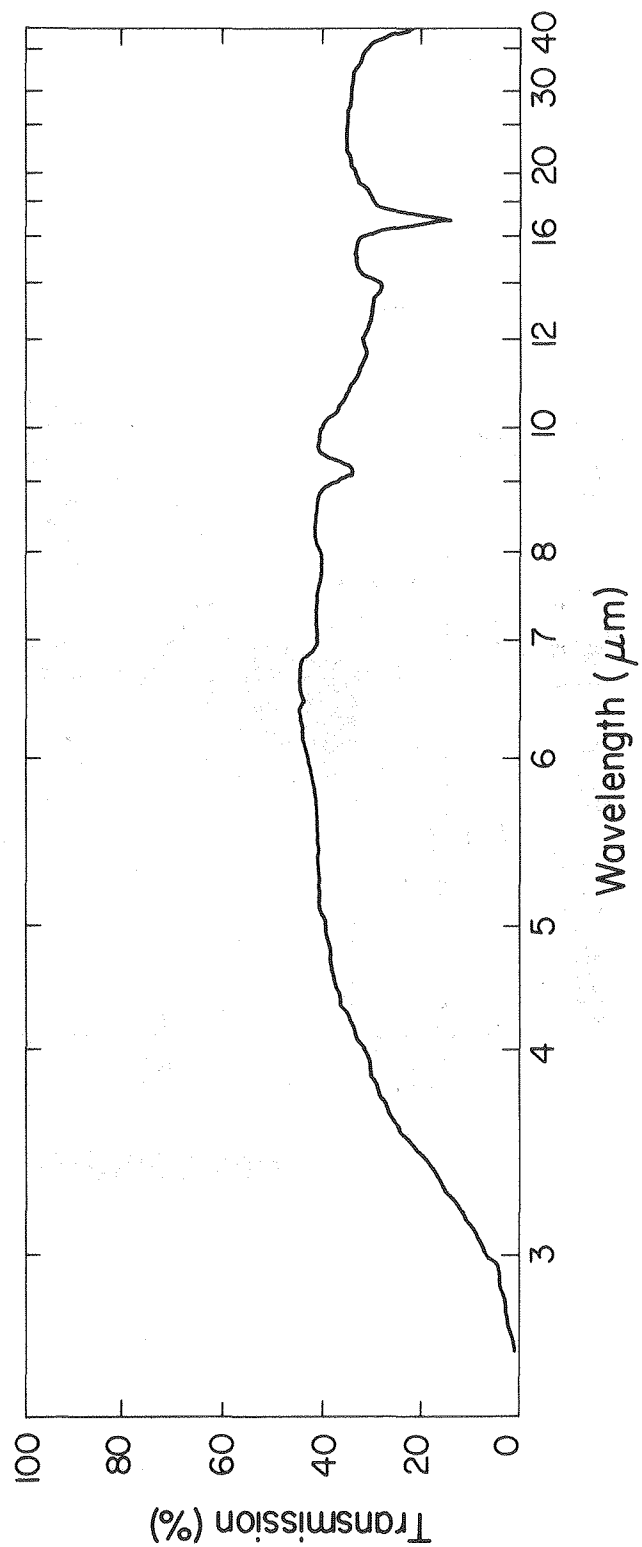
XBL 813-525

Figure 9.



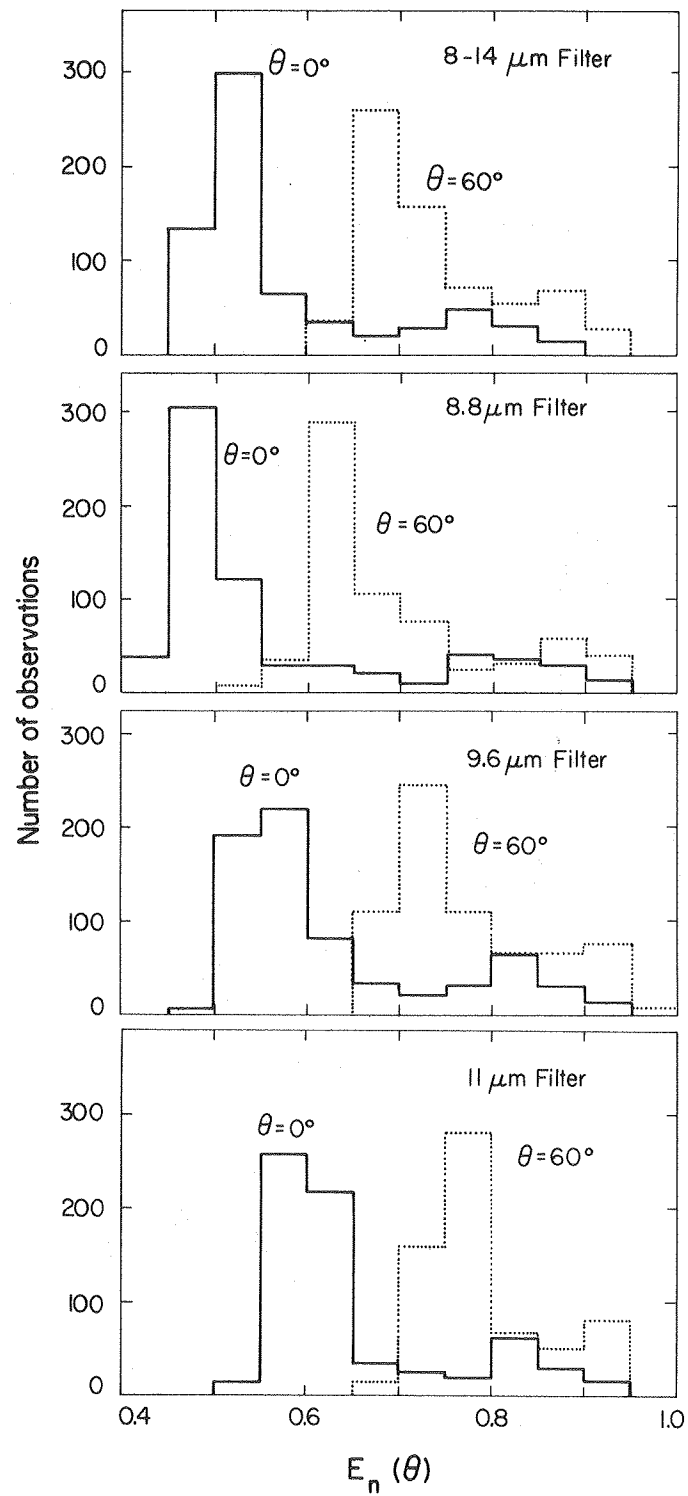
XBL 813-526

Figure 10.



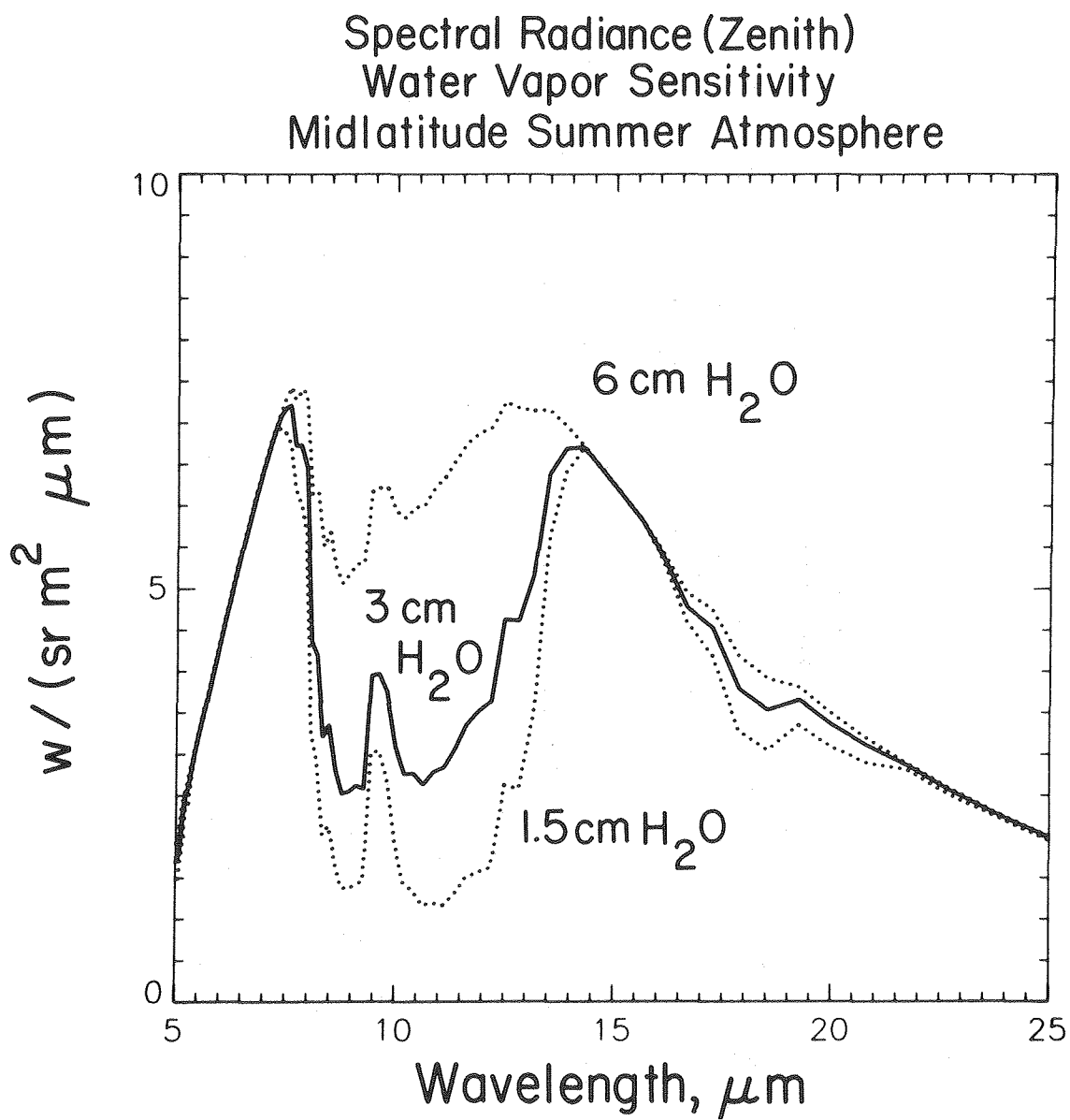
XBL 813-527

Figure 11.



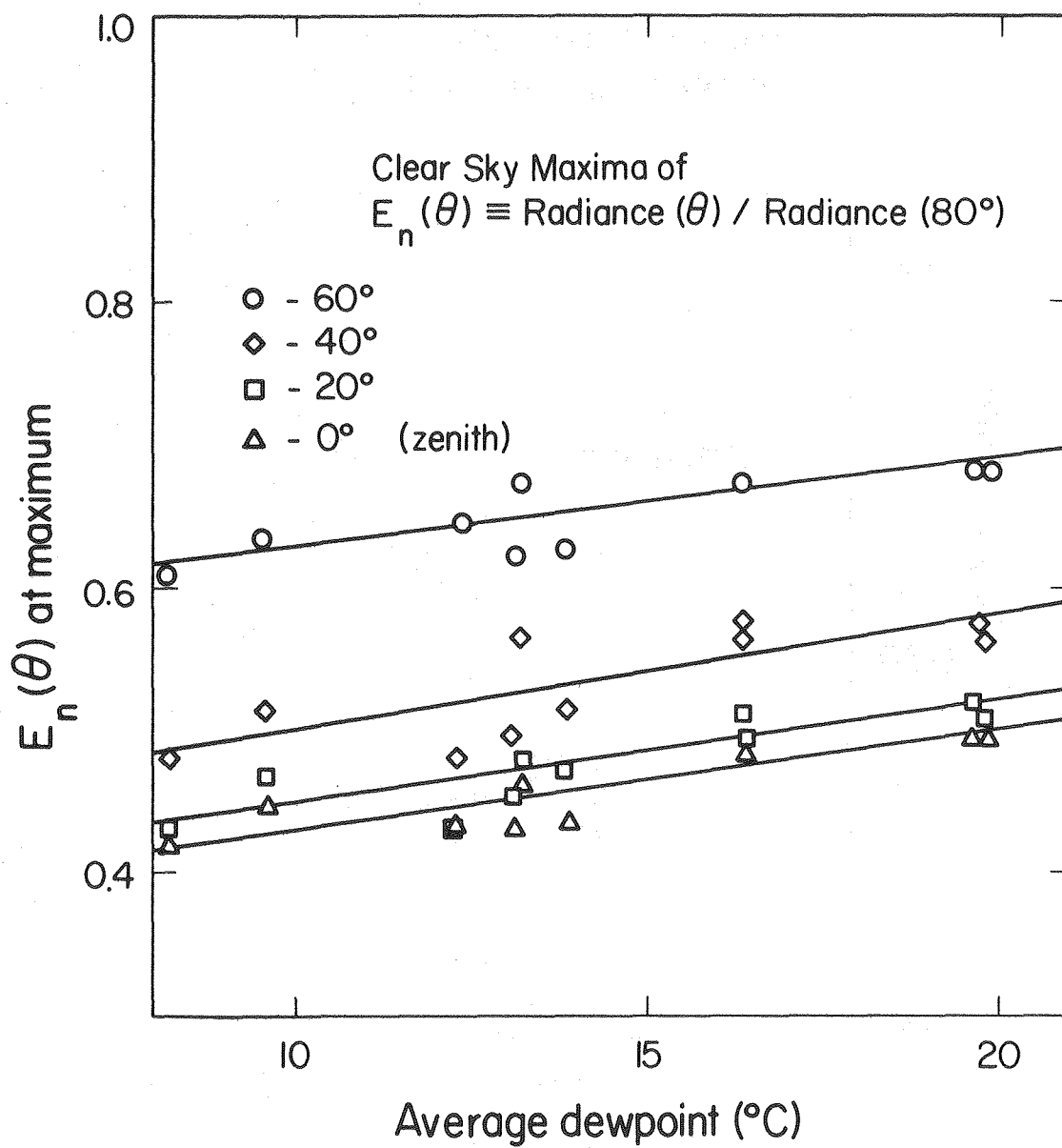
XBL 813-529

Figure 12.



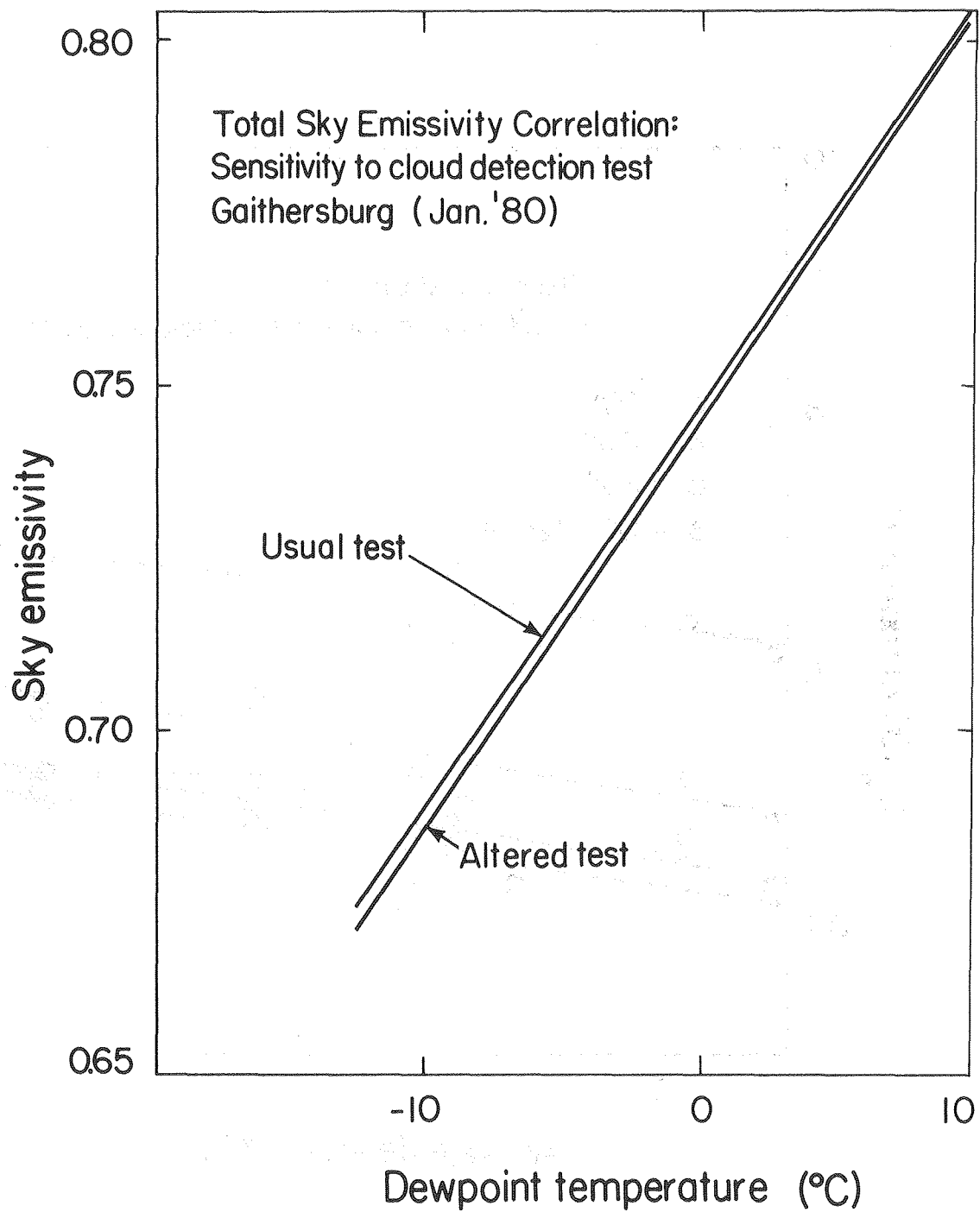
XBL 83I-530

Figure 13.

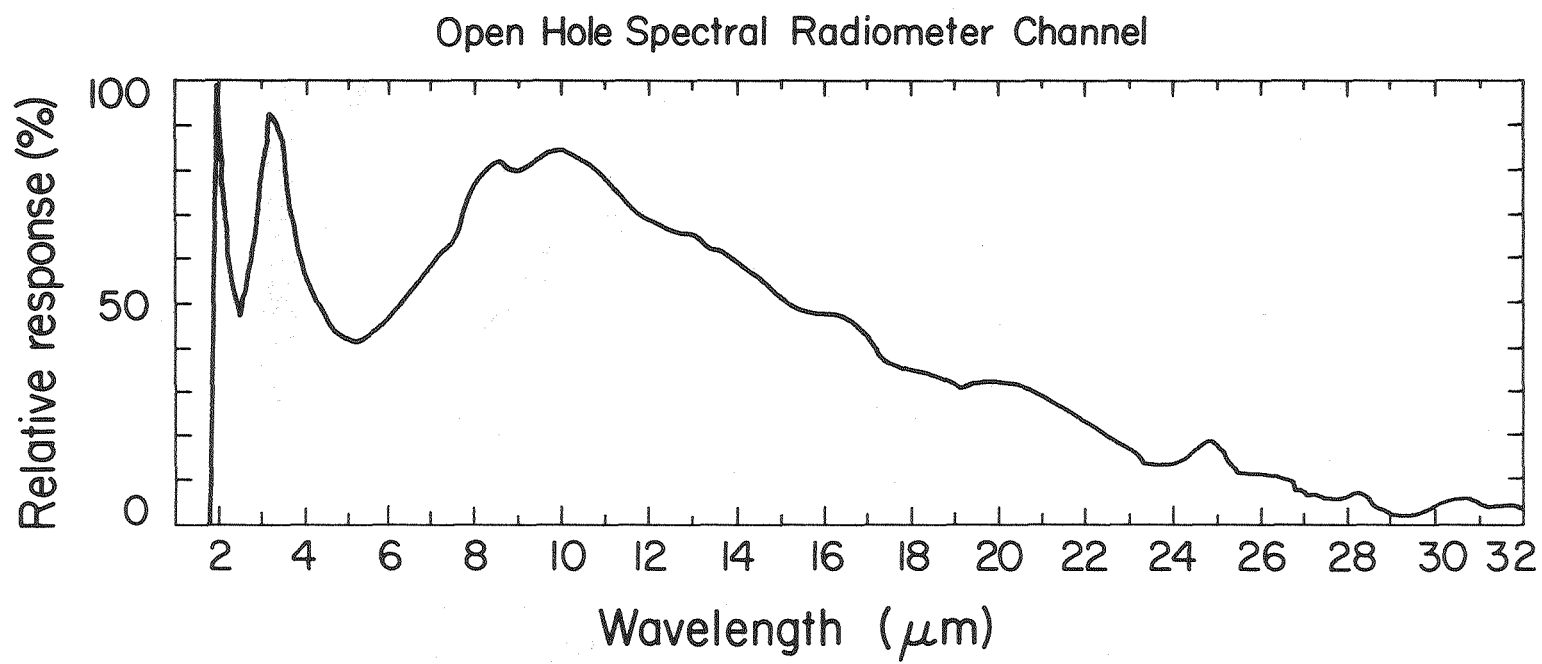


XBL 813-531

Figure 14.



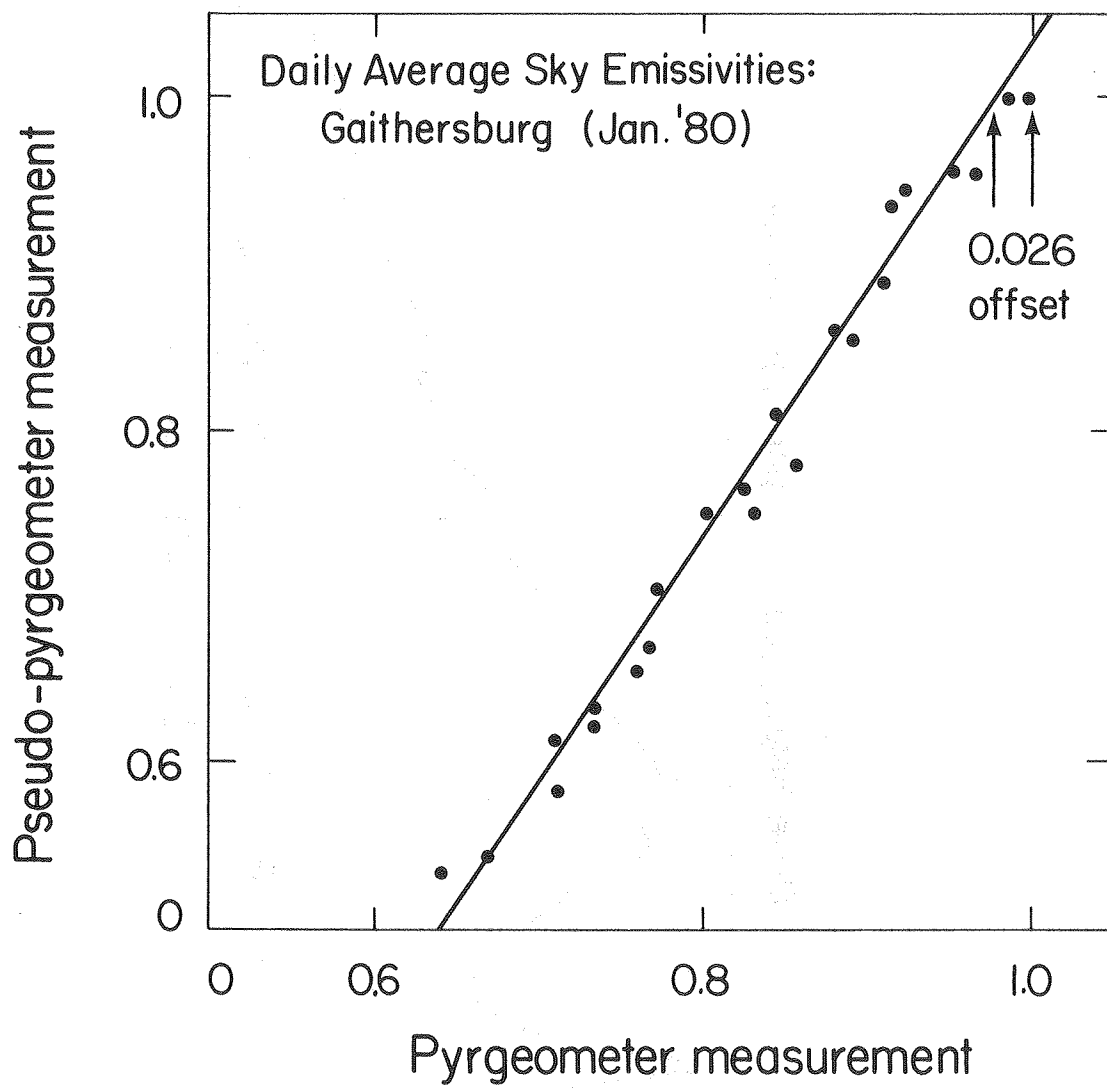
XBL 813-532



XBL 813-533

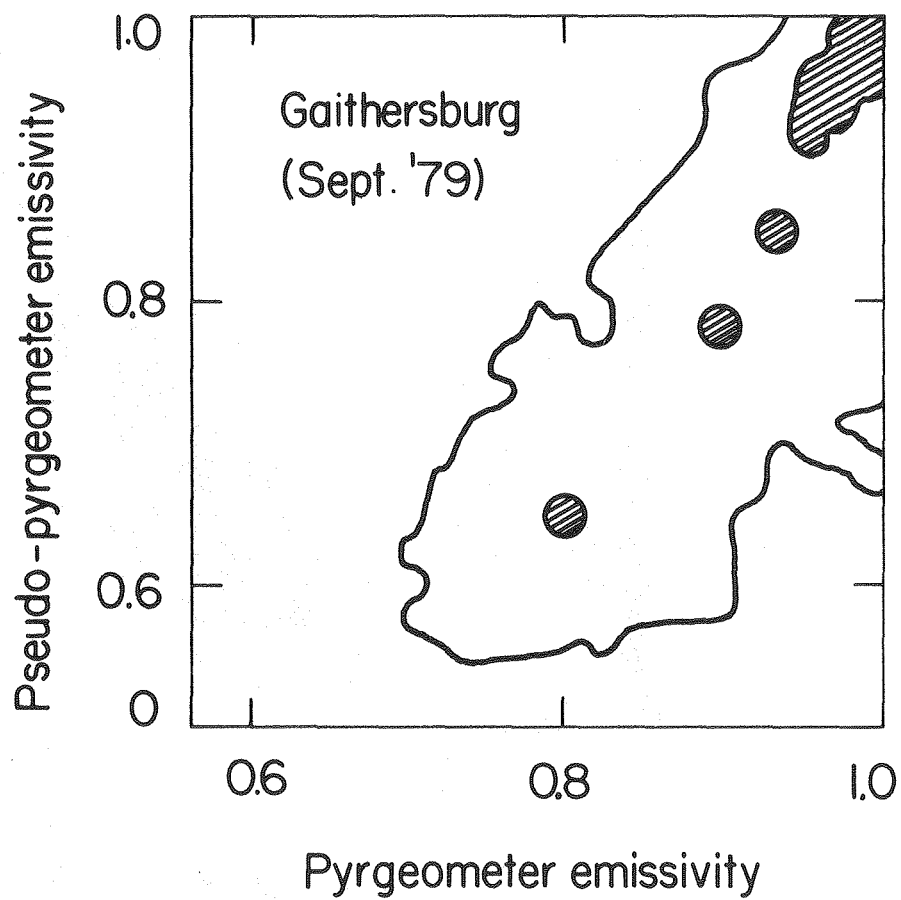
Figure 15.

Figure 16.



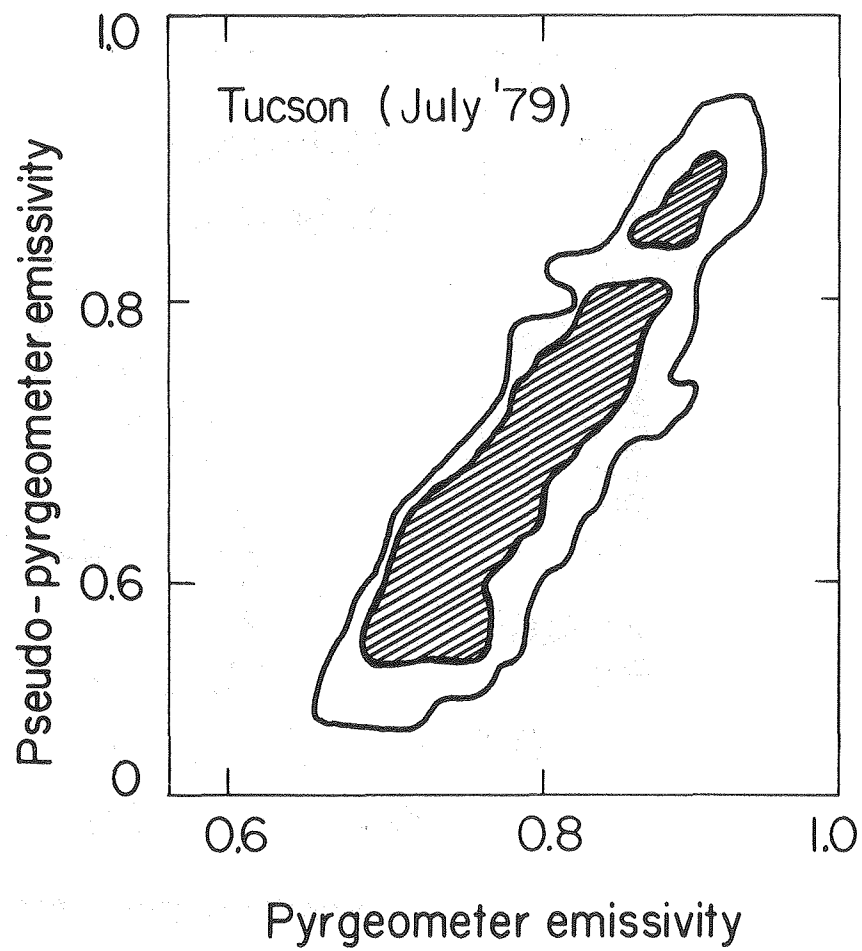
XBL 813-534

Figure 17.



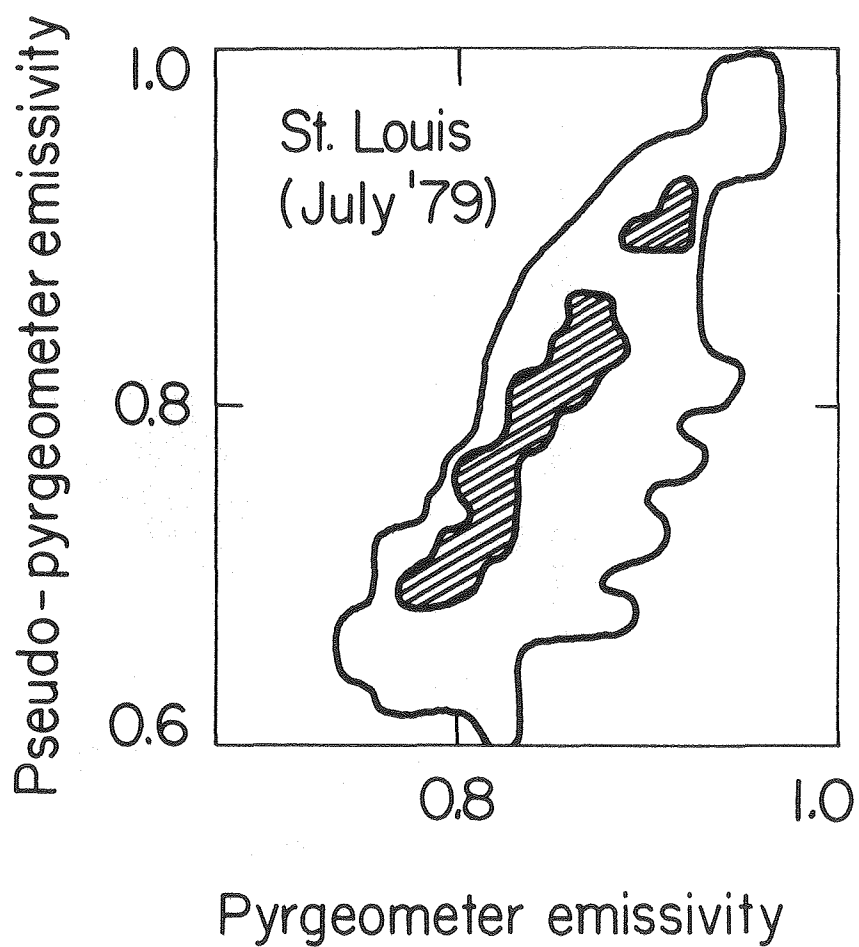
XBL813-535

Figure 18.



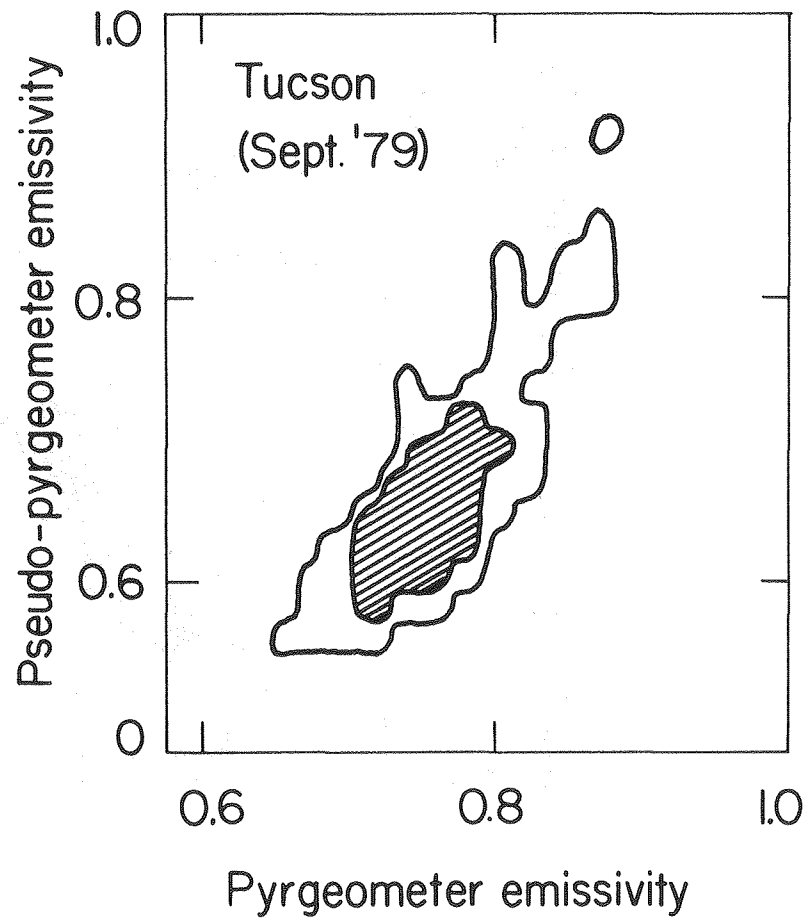
XBL 813-536

Figure 19.



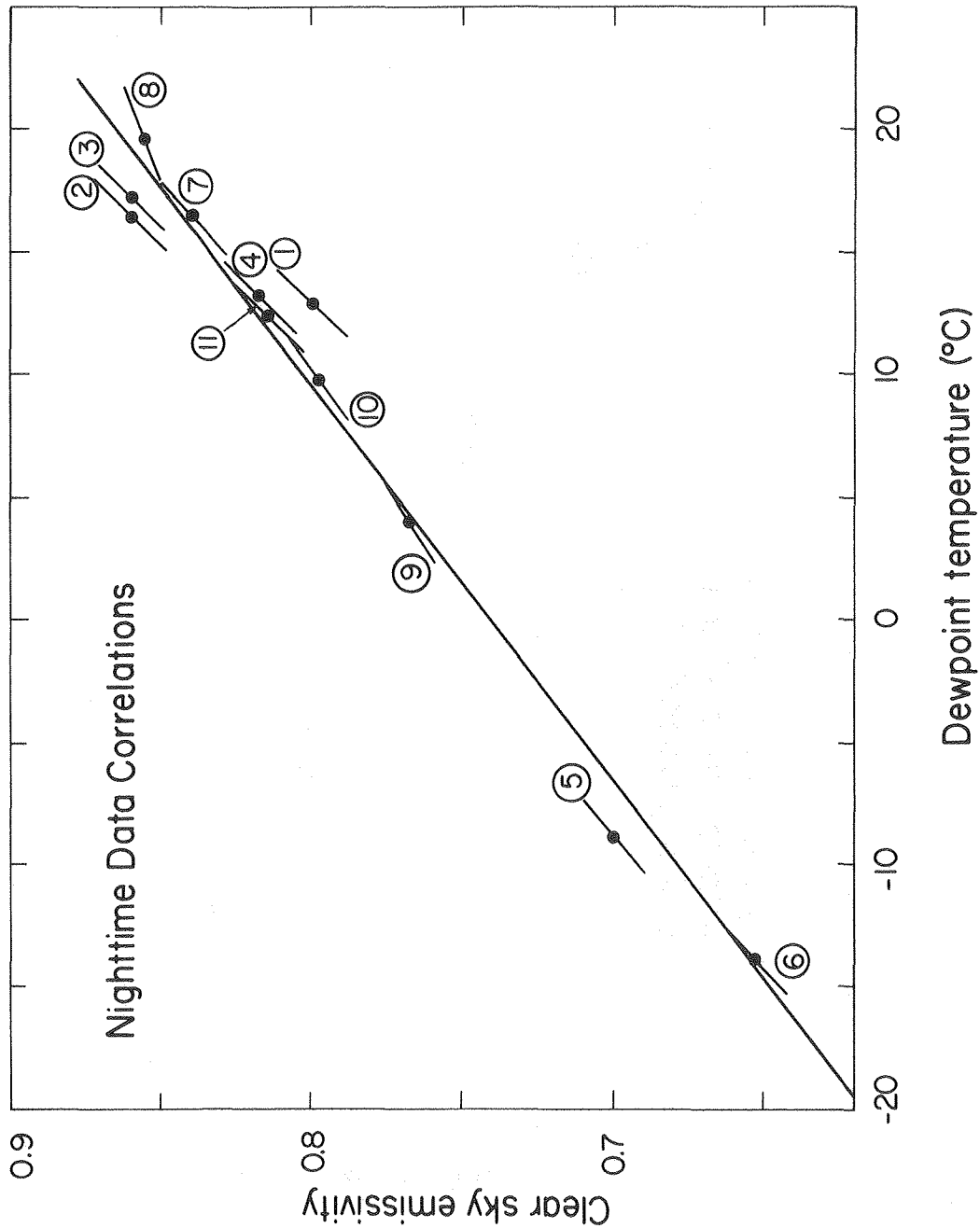
XBL 813-537

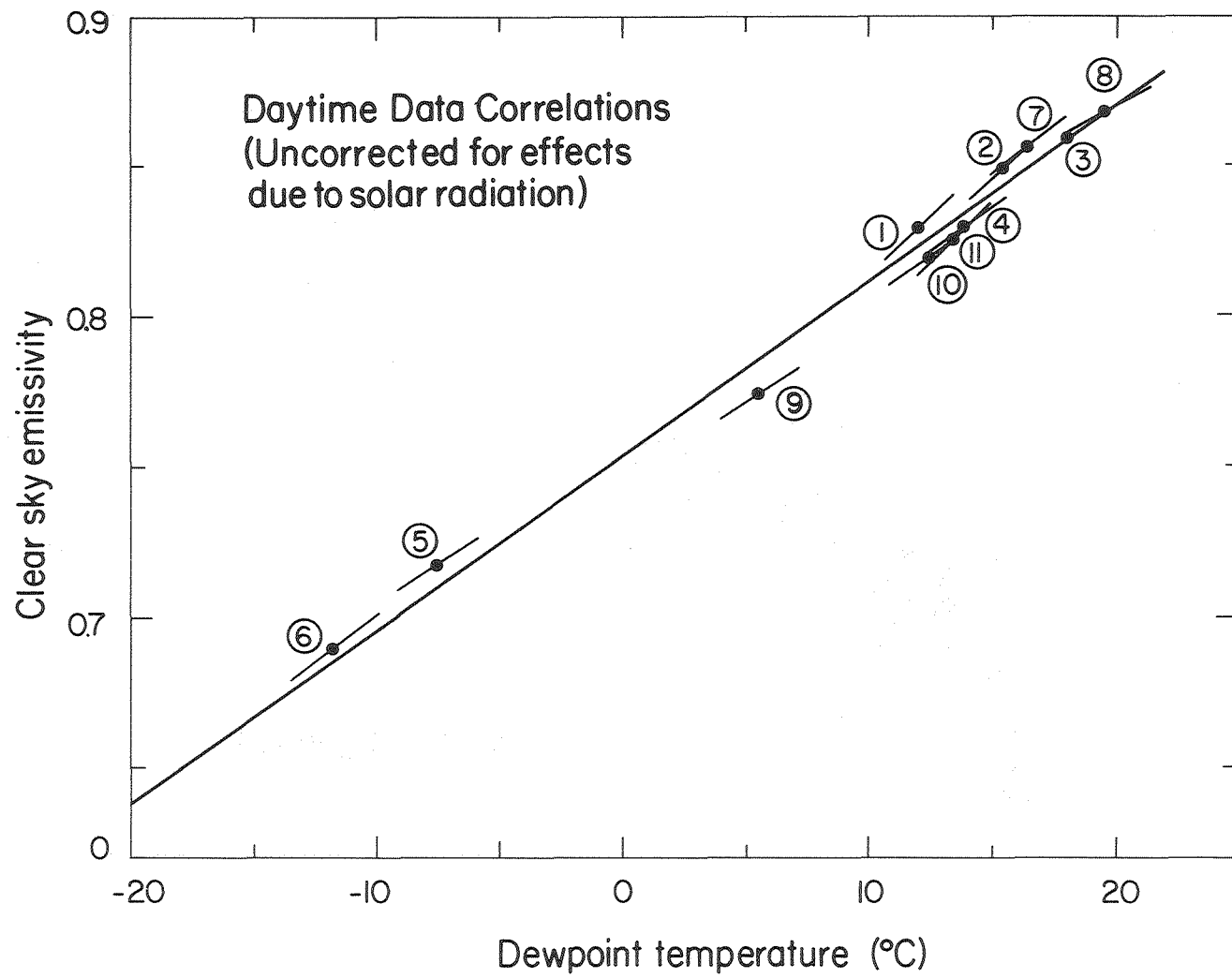
Figure 20.



XBL 813-538

Figure 21.





XBL 813-540

Figure 22.

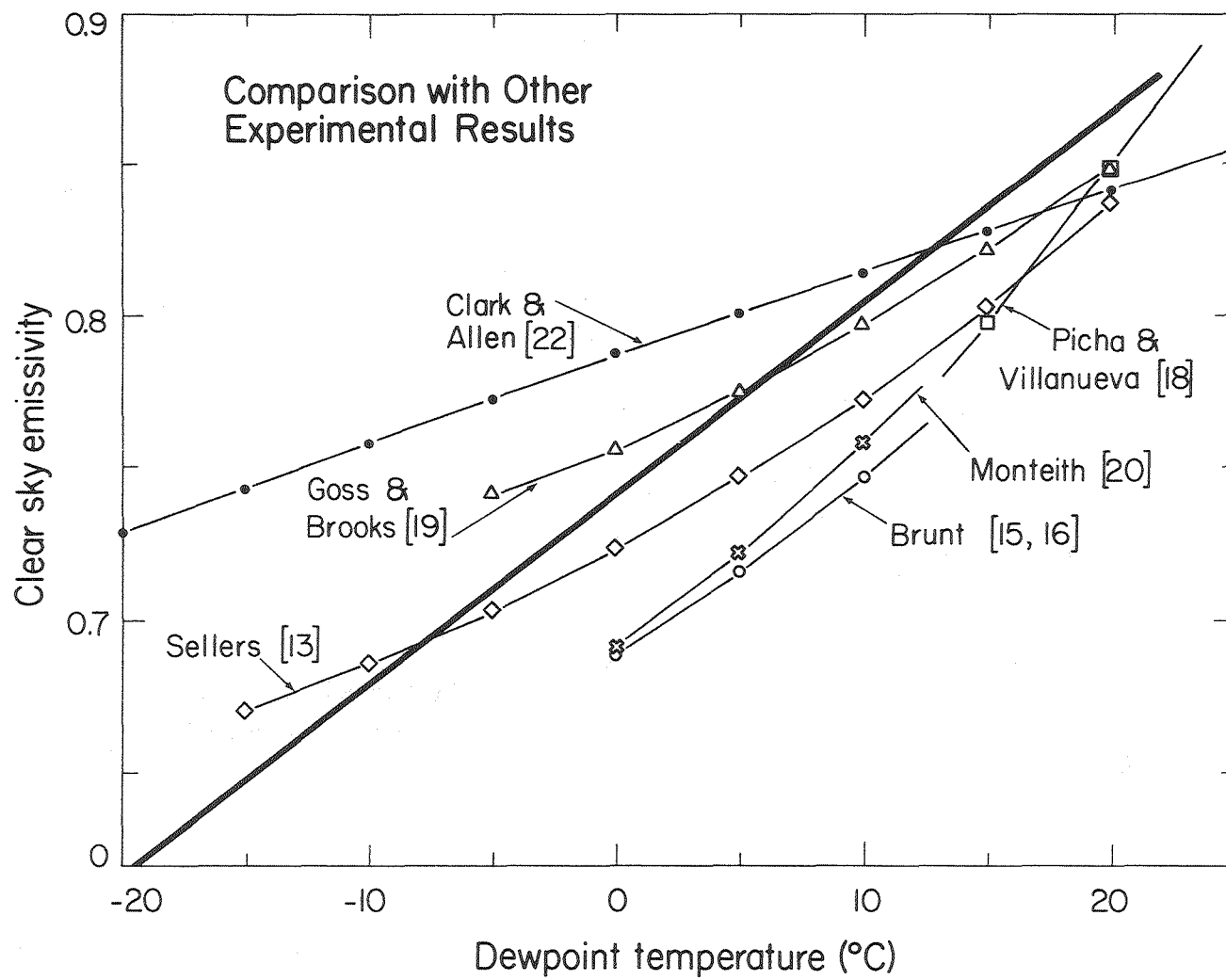


Figure 23.

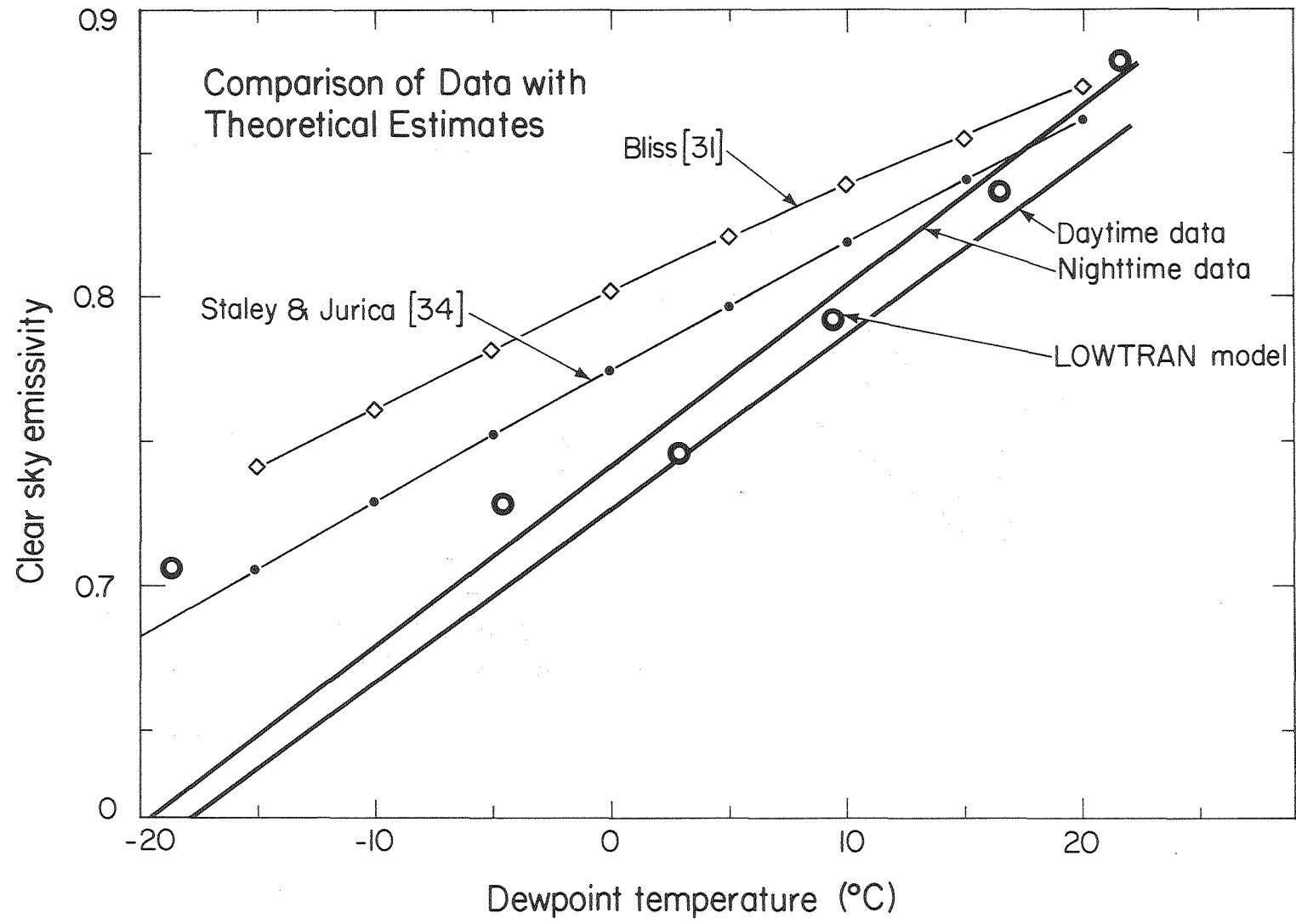


Figure 24.

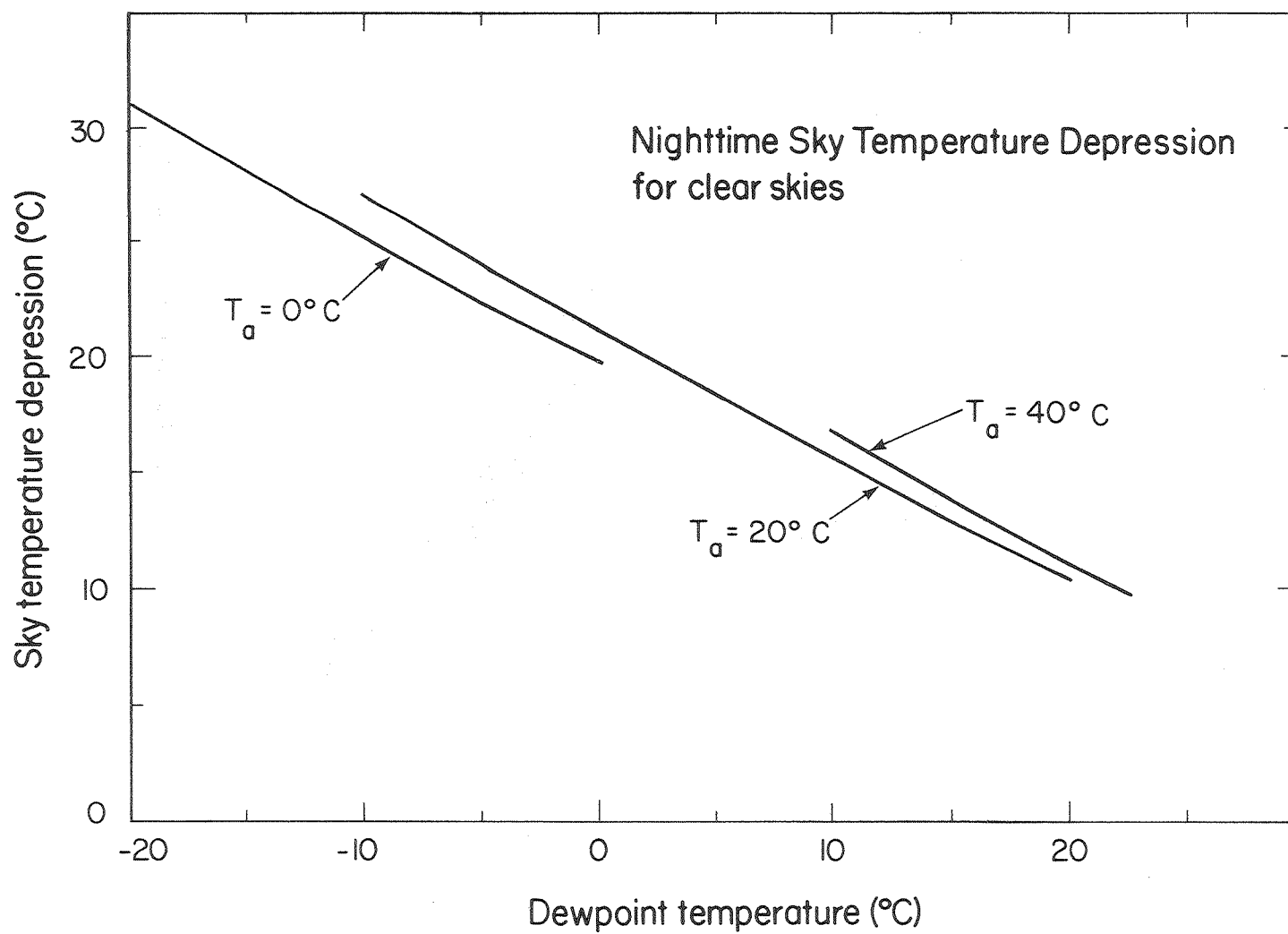
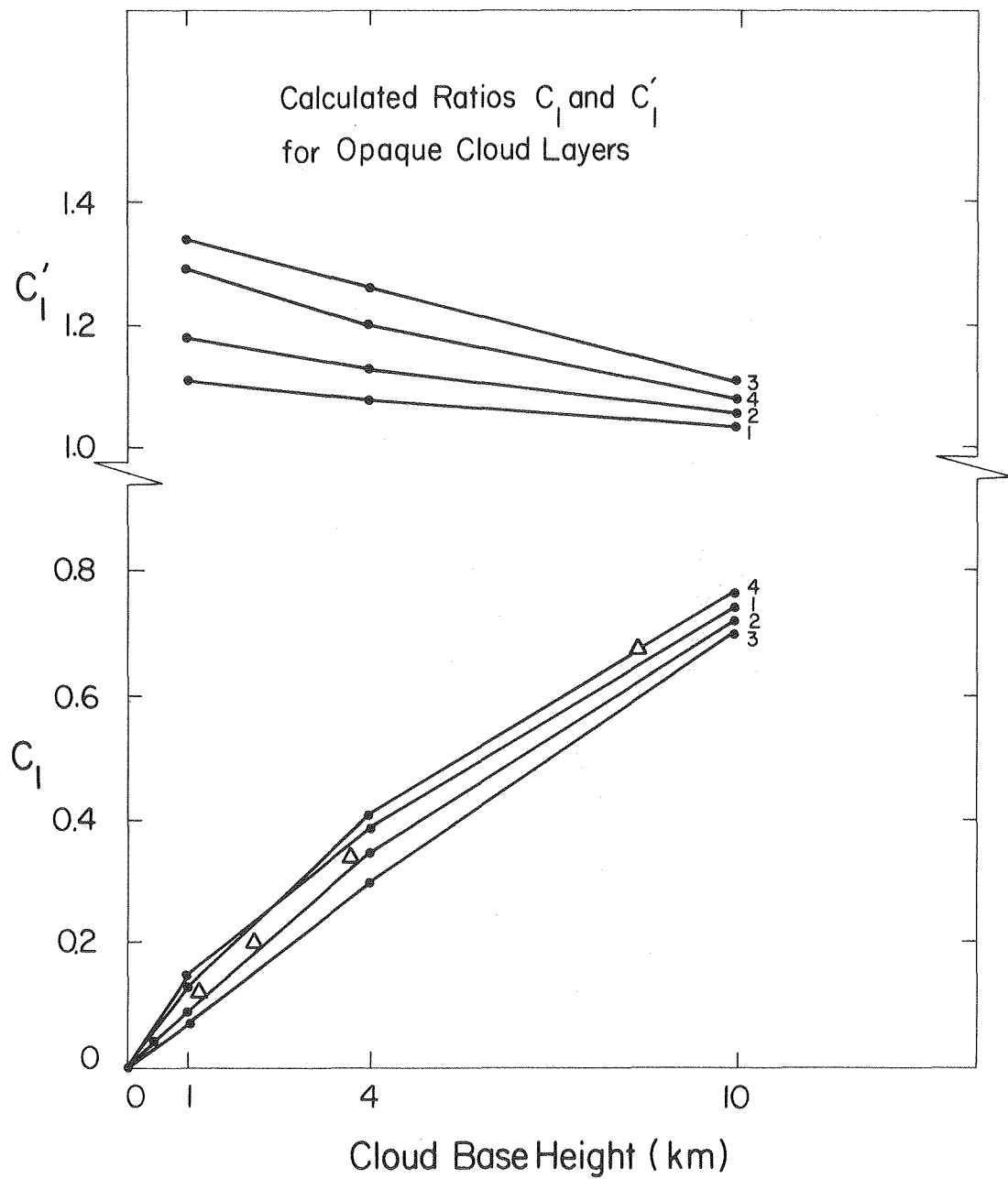


Figure 25.

Figure 26.



XBL 813-544